

# Numerical simulations of flow past three circular cylinders in equilateral-triangular arrangements

Weilin Chen<sup>1</sup>, Chunnging Ji<sup>1,2,†</sup>, Md. Mahbub Alam<sup>3</sup>, John Williams<sup>4,5</sup>  
and Dong Xu<sup>1,2</sup>

<sup>1</sup>State Key Laboratory of Hydraulic Engineering Simulation and Safety, Tianjin University, Tianjin 300350, China

<sup>2</sup>Key Laboratory of Earthquake Engineering Simulation and Seismic Resilience of China Earthquake Administration, Tianjin University, Tianjin 300350, China

<sup>3</sup>Institute for Turbulence-Noise-Vibration Interaction and Control, Harbin Institute of Technology (Shenzhen), Shenzhen, 518055, China

<sup>4</sup>School of Engineering and Material Science, Queen Mary University of London, London E1 4NS, UK

<sup>5</sup>State Key Laboratory of Hydraulics and Mountain River Engineering, Sichuan University, Chengdu 610065, China

(Received 23 May 2019; revised 22 November 2019; accepted 8 February 2020)

Flow past three identical circular cylinders is numerically investigated using the immersed boundary method. The cylinders are arranged in an equilateral-triangle configuration with one cylinder placed upstream and the other two side-by-side downstream. The focus is on the effect of the spacing ratio  $L/D$  ( $= 1.0$ – $6.0$ ), Reynolds number  $Re$  ( $= 50$ – $300$ ) and three-dimensionality on the flow structures, hydrodynamic forces and Strouhal numbers, where  $L$  is the cylinder centre-to-centre spacing and  $D$  is the cylinder diameter. The fluid dynamics involved is highly sensitive to both  $Re$  and  $L/D$ , leading to nine distinct flow structures, namely single bluff-body flow, deflected flow, flip-flopping flow, steady symmetric flow, steady asymmetric flow, hybrid flow, anti-phase flow, in-phase flow and fully developed in-phase co-shedding flow. The time-mean drag and lift of each cylinder are more sensitive to  $L/D$  than  $Re$  while fluctuating forces are less sensitive to  $L/D$  than  $Re$ . The three-dimensionality of the flow affects the development of the wake patterns, changing the  $L/D$  ranges of different flow structures. A diagram of flow regimes, together with the contours of hydrodynamic forces, in the  $Re - L/D$  space, is given, providing physical insights into the complex interactions of the three cylinders.

**Key words:** vortex dynamics, vortex interactions, wakes

## 1. Introduction

Multiple cylindrical structures (e.g. heat exchanger tubes, marine riser bundles and undersea pipelines) are more frequently encountered in engineering practices than isolated ones, although less attention has been paid to the hydrodynamics of these multi-structure systems. While the flow around two cylinders has been investigated

† Email address for correspondence: [cnji@tju.edu.cn](mailto:cnji@tju.edu.cn)

extensively, little attention has been paid to the flow around three circular cylinders. In this paper, the hydrodynamic forces, spectral features and wake structures of three cylinders in an equilateral configuration are investigated in a large parametric space to provide a thorough understanding of the underlying physics of fluid dynamics.

Due to the complexity of the problem, the flow past two circular cylinders is reviewed first. Zdravkovich (1977) classified the two-cylinder flow interference into proximity interference, wake interference and combined interference. For the flow around two tandem cylinders, three distinct flows (i.e. extended, reattachment and co-shedding) are observed based on the spacing ratio  $L/D$  (Zdravkovich 1987; Alam *et al.* 2003b; Papaioannou *et al.* 2006; Sumner 2010; Alam 2014), where  $L$  is the centre-to-centre spacing of the cylinders and  $D$  is the cylinder diameter. The extended-body flow appears at  $L/D < 1.2$ – $1.8$  where the two cylinders are so close to each other that the free shear layers separating from the upstream cylinder overshoot the downstream one, and the flow in the cylinder gap is stagnant. In the reattachment case ( $1.2$ – $1.8 < L/D < 3.4$ – $3.8$ ), the shear layers separating from the upstream cylinder reattach on the downstream cylinder and the flow in the gap is quasi-steady. The co-shedding flow materializes at  $L/D > 3.4$ – $3.8$ , where the shear layers roll up alternately in the gap between the cylinders and thus the flow in the gap is significantly unsteady. The  $L/D$  separating the reattachment and co-shedding flows is known as the critical spacing. Note that the critical spacing is affected by many factors, such as the Reynolds number ( $Re$ ), turbulence intensity of the incoming flow, etc. (Ljungkrona, Norberg & Sunden 1991; Alam 2014). A hysteresis behaviour was observed between the reattachment and co-shedding regimes for increasing and decreasing  $L/D$  and  $Re$  (Igarashi 1981; Liu & Chen 2002). In the transition from the reattachment to co-shedding patterns, the fluid forces and Strouhal ( $St$ ) number jump from small to high values. Concomitantly, the mean drag coefficient leaps from a negative value to a positive value – termed the drag inversion (Carmo, Meneghini & Sherwin 2010). For all three regimes, the upstream cylinder significantly affects the flow around the downstream cylinder even at very large  $L/D$ . However, the effect of the downstream cylinder on the upstream one is only perceivable for  $L/D < 5.0$  (Papaioannou *et al.* 2006).

For the side-by-side arrangement of two cylinders, the proximity interference occurs when the cylinders are close to each other. Five flow patterns were summarized in Sumner (2010). When  $L/D$  is small ( $L/D < 1.1$ – $1.2$ ), no gap flow exists between the cylinders and vortices are alternately shed from the free-stream sides of the cylinders (Alam, Moriya & Sakamoto 2003a). The two cylinders behave like a single bluff body. For intermediate  $L/D$  ( $1.1$ – $1.2 < L/D < 2.0$ – $2.2$ ), the gap flow is weak, and two flow patterns, i.e. the deflected flow (DF) pattern and the flip-flopping (FF) pattern, intermittently appear. It is noted that the FF pattern shows clearly different characteristics between the low- $Re$  laminar flow and high- $Re$  turbulent flow. Kim & Durbin (1988) ( $Re = 1.9 \times 10^3$ – $6.9 \times 10^3$ ) found that the flip-over time interval of the gap flow is several orders of magnitude longer than the vortex-shedding period. On the other hand, for low- $Re$  flow ( $Re = 40$ – $160$ ), the time scale is only a few vortex-shedding periods (Kang 2003; Carini, Giannetti & Auteri 2014b). When  $L/D$  is large ( $> 2.0$ – $2.5$ ), in-phase or anti-phase flow patterns appear depending upon  $L/D$  (Williamson 1985). In these two patterns, the flow interference between the cylinders is weak. Kang (2003) numerically simulated the flow past two side-by-side cylinders at  $Re = 40$ – $160$ ,  $L/D = 1.0$ – $6.0$ , and his results showed six distinct near-wake patterns: anti-phase, in-phase, flip-flopping, deflected, single bluff-body and steady. Liu *et al.* (2007), in their numerical study of flow past two side-by-side cylinders

at  $Re = 18$ – $100$ , further classified the near wake into nine patterns, including four steady ones (single bluff body, separated double body, transition and biased) and five unsteady ones (single bluff body, biased quasi-steady, flip-flopping, in-phase and anti-phase). Supradeepan & Roy (2014) numerically investigated the near-wake patterns behind two side-by-side cylinders at  $Re = 100$  and  $L/D = 1.1$ – $8.0$ . They found that there exist five flow regimes, namely single bluff-body periodic ( $L/D = 1.1$ – $1.3$ ), aperiodic ( $L/D = 1.4$ – $2.2$ ), transiting ( $L/D = 2.3$ – $3.1$ ), anti-phase ( $L/D = 3.2$ – $7.9$ ) and in-phase ( $L/D > 8.0$ ).

For staggered arrangements of the two cylinders, all three kinds of flow interference (proximity, wake and combined interference) can be observed based on the angle of attack  $\alpha$  and  $L/D$ . Zdravkovich (1987) experimentally observed two flow regimes for the flow past two staggered cylinders at high Reynolds numbers, i.e. a gap flow regime where an attractive lift appears and a wake displacement regime where a repulsive lift occurs. Akbari & Price (2005) found five different flow regimes in their numerical simulations of the flow past two staggered circular cylinders at  $Re = 800$ . They were named the base bleed ( $L/D \leq 1.1$  and  $\alpha \geq 30^\circ$ ), shear layer reattachment ( $1.1 < L/D < 2.0$  and  $\alpha < 10^\circ$ ), vortex pairing and enveloping ( $1.0 \leq L/D \leq 2.0$  and  $\alpha \geq 30^\circ$ ), vortex impingement ( $L/D \geq 3.0$  and  $\alpha \leq 10^\circ$ ) and complete vortex-shedding ( $L/D \geq 2.5$  and  $\alpha \geq 30^\circ$ ) flow regimes, respectively. Alam & Sakamoto (2005) experimentally investigated the flow past two staggered circular cylinders at  $Re = 5.5 \times 10^4$ . A number of discontinuities in the flow were observed when  $\alpha$  and/or  $L/D$  were varied. Alam & Meyer (2013) identified that two cylinders interact with each other in six different interaction mechanisms, depending on  $\alpha$  and  $L/D$ . These were termed boundary layer–cylinder interaction, shear layer or wake–cylinder interaction, shear layer–shear layer interaction, vortex–cylinder interaction, vortex–shear layer interaction, and vortex–vortex interaction. While the vortex–cylinder interaction resulted in a very high fluctuating drag, vortex–shear layer interaction engendered a high fluctuating lift. Tong, Cheng & Zhao (2015) provided detailed physics in the flow past two staggered circular cylinders through a set of direct numerical simulations with  $Re = 10^3$ . They found a strong flow three-dimensionality in the gap between the cylinders.

The flow around three cylinders is more complex than that around two. Igarashi & Suzuki (1984) experimentally studied the characteristics of flow around three tandem cylinders with  $L/D = 1.0$ – $4.0$  and  $Re = 1.09 \times 10^4$ – $3.92 \times 10^4$ . On account of the dynamic effects of the upstream-cylinder shear layers on the downstream cylinders, six flow patterns and two bistable flow regions were identified. Harichandan & Roy (2010) numerically investigated the flow past three stationary tandem cylinders with  $L/D = 2.0$  and  $5.0$  at  $Re = 100$  and  $200$ . Results showed that the downstream cylinder experiences large unsteady forces that can give rise to a wake-induced flutter if the downstream cylinder is free to vibrate.

Moreover, Kang (2004) numerically simulated laminar flow past three side-by-side cylinders at  $Re = 100$  and found that the flow patterns can be summarized into five different kinds based on  $L/D$ . These are single bluff body ( $L/D < 1.3$ ), deflected ( $L/D \approx 1.3$ ), flip-flopping ( $1.3 < L/D \leq 2.2$ ), in-phase ( $L/D \approx 2.5$ ) and modulation ( $L/D \geq 3.0$ ). For the modulation pattern, the vortex-shedding frequency of the central cylinder is slightly larger than that of a side cylinder, and the modulation period is long. Han, Zhou & Tu (2013) carried out numerical simulations of the flow past three side-by-side cylinders at  $Re = 40$ – $160$  which produced eight flow patterns: single bluff body, deflected, flip-flopping, non-identical and identical steady patterns, anti-phase and in-phase patterns and a combined pattern (consisting of the in-phase and anti-phase patterns). In their low- $Re$  cases, asymmetric and symmetric steady patterns were

observed. Specifically, when  $L/D$  is small, vorticities in the gap shear layers are much lower than those in the free-stream shear layers. However, when  $L/D$  is large enough, three cylinders behave as isolated cylinders, and the vorticity field and hydrodynamic forces are the same for the three cylinders.

Flow past four cylinders in square arrangements has also been investigated by several researchers. Sayers (1990) showed in their wind tunnel experiments that, for  $L/D \geq 4.0$ , the frequency of vortex shedding from each of the four cylinders is similar to that of an isolated cylinder. Esfahani & Vasel-Be-Hagh (2010) numerically demonstrated that there are three different flow patterns in the range of  $L/D = 1.5$ – $4.5$ , i.e. stable shielding flow, wiggling shielding flow and vortex-shedding flow. The critical spacing ratios between them are  $L/D = 2.5$  and  $3.5$ , respectively. Results of Lam, Li & So (2003) showed three flow patterns at  $Re = 2.25 \times 10^4$ – $5.18 \times 10^4$ . Recently, Esfahani & Vasel-Be-Hagh (2013) found that there exists a transition between the anti-phase and in-phase patterns within the range of  $L/D = 2.0$ – $3.0$  at  $Re = 200$ .

Yang *et al.* (2016) studied the flow past three circular cylinders in equilateral-triangular arrangements at  $Re = 50$ – $200$  from the viewpoint of vortex-shedding suppression. Their results showed that, at  $\alpha = 0^\circ$  (one upstream cylinder and the other two side-by-side downstream), the vortex shedding from the upstream cylinder is suppressed for  $Re = 100$ – $200$ . However, when  $\alpha = 60^\circ$  (two upstream cylinders in side-by-side and one downstream cylinder), the suppression occurs on the downstream cylinder at  $Re \leq 175$ . de Paula, Endres & Möller (2013) experimentally identified the bistable phenomenon at  $L/D = 1.6$  and  $\alpha = 0^\circ$ . Zheng, Zhang & Lv (2016) numerically investigated the flow past three equidistantly arranged cylinders at  $Re = 100$  and  $200$  with  $L/D = 1.5$ – $7.0$ . The deflected pattern appears when  $\alpha = 0^\circ$ , which is consistent with the findings in Yang *et al.* (2016). Moreover, the deflected pattern shows a clear dependence on  $Re$ : it disappears at  $L/D \geq 2.0$  when  $Re = 100$  and at  $L/D \geq 3.0$  when  $Re = 200$ . Bao, Zhou & Huang (2010) numerically investigated the same problem for  $L/D = 1.5$ – $5.0$ ,  $\alpha = 0^\circ$ – $60^\circ$  and  $Re = 100$ . Five flow patterns were confirmed, i.e. single bluff body, deflected, flip-flopping, in-phase and anti-phase. Moreover, they found that the flow interference between the three cylinders plays an important role in the variation of lift frequency. At a high  $Re = 6.2 \times 10^4$ , Tatsuno, Amamoto & Ishi-i (1998) experimentally studied the flow interference between three cylinders at  $\alpha = 0^\circ$ – $60^\circ$ ,  $L/D = 1.39$ – $6.93$ . When  $L/D$  is small ( $< 2.6$ ), the interference is strong, leading to an asymmetric wake. On the other hand, at  $L/D \geq 3.5$ , the flow interference is weak and the wake becomes symmetric. Bansal & Yarusevych (2017) found a bistable flow pattern at  $\alpha = 0^\circ$ ,  $L/D = 1.35$  and  $Re = 2.1 \times 10^3$ , without the switching of the gap flow direction. The biased direction of the gap flow is dependent on the initial flow conditions. This is consistent with the results of Lam & Cheung (1988) at  $Re = 2.1 \times 10^3$ – $3.5 \times 10^3$ , where the bistable pattern appears when  $L/D \leq 2.29$  at  $\alpha = 0^\circ$ .

By comparing with the flow around a single or a pair of cylinders, the flow past three equilateral-triangular-arranged circular cylinders is not well-investigated. Researchers have only carried out studies on the flow past three equispaced cylinders within a narrow parametric space. A systematic study on the flow around three cylinders and its dependence on  $Re$  and  $L/D$  is still missing. The main objectives of this investigation are to establish an overall and comprehensive understanding of this problem in a wider parametric space of  $L/D = 1.0$ – $6.0$  and  $Re = 50$ – $300$  with fine increments in both  $L/D$  and  $Re$ , and to inspect the influences of the wake three-dimensionality by performing three-dimensional direct numerical simulations.

The remains of the paper are organized as follows. In § 2, the adopted numerical methodology and the validation cases are presented. Section 3 presents the effects of the spacing ratio on flow features and hydrodynamics. The wake pattern, the drag and lift forces and the spectral frequency are discussed. The key roles of the Reynolds number are further elucidated in § 4. Section 5 discusses the flow regime partition in the  $Re - L/D$  parametric space, while § 6 inspect the influences of the wake three-dimensionality. The main conclusions are summarized in § 7.

## 2. Numerical methodology and validation cases

The governing equations for the fluid flow are the incompressible Navier–Stokes equations. The two-step predictor–corrector procedure is adopted for the decoupling of the flow governing equations, and the resulting pressure Poisson equation is solved by using the biconjugate gradients stabilized method and the multi-grid method. The second-order Adams–Bashforth time marching scheme is employed to calculate a new velocity field.

The flow around the cylinders is simulated by using the immersed boundary (IB) method which was first introduced by Peskin (1972) in the simulation of blood flow around the leaflet of a human heart. In the framework of the IB method, the flow governing equations are discretized on a fixed Cartesian grid, which generally does not conform to the geometry of the cylinders. As a result, the boundary conditions on the fluid–cylinder interface cannot be imposed directly. Instead, an extra body force is added into the momentum equation to take such interaction into account. One of the advantages of the IB method lies in its parameterized and fast implementation of a large number of cases with different geometric configurations, compared with conventional methods using body-conformal grids. For the sake of conciseness, details of the methodology are not presented here and readers are referred to our previous work (Ji, Munjiza & Williams 2012; Chen *et al.* 2015*b*; Chen, Ji & Xu 2019) for further information.

The arrangement of the cylinders in the computational domain is presented in figure 1, where Cylinders 1, 2 and 3 are arranged in an equilateral triangle with Cylinder 1 placed upstream and Cylinders 2 and 3 side-by-side downstream. The spacing between the centres of two cylinders is defined as  $L$  and is varied from 1.0 to 6.0. The computational domain is  $200D \times 200D$ . The centre of the computational domain coincides with the centre of the triangle formed by the cylinder centres (figure 1). The origin of the  $(x, y)$  coordinate system is also located at the centre of the triangle. The smallest normalized grid spacing is set to  $\Delta x/D = \Delta y/D = 1/64$  in a region of  $8D \times 8D$  surrounding the cylinders. This grid resolution has been demonstrated to be sufficiently fine by Chen *et al.* (2015*a,b*, 2018). A Dirichlet-type boundary condition is adopted at the inflow and a Neumann-type boundary condition is employed at the outflow. The top and bottom walls are set as free-slip boundaries. To capture the long-period flow pattern, the two-dimensional (2-D) simulations are carried out for a non-dimensional time  $t^* = tU/D > 5000$ , after a statistically stable flow state has been reached, where  $U$  is the free-stream flow velocity.

In this study, the numerical methodology is validated for an isolated cylinder at  $Re = 50$ –200 (table 1), two side-by-side cylinders at  $L/D = 2.5$  and  $Re = 100$  (table 2) and three cylinders in an equilateral-triangular arrangement at  $L/D = 3.0$  and  $Re = 100$  (table 3) where the time-mean drag coefficient  $\overline{C_d}$ , fluctuating root-mean-square (r.m.s.) lift coefficient  $C_l'$  and Strouhal number  $St$  are presented and compared with those in the literature. In table 1, the maximum discrepancy between the results is marginal, confirming a reasonably high accuracy of the adopted numerical methodology for the

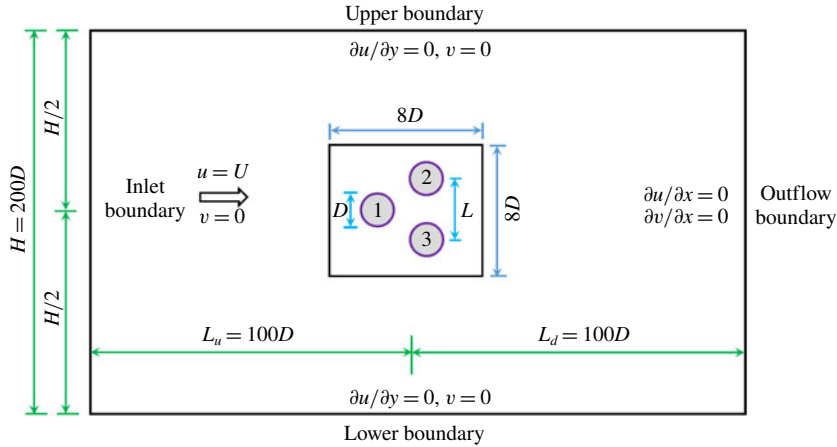


FIGURE 1. The computational domain and boundary conditions for the flow past three cylinders in an equilateral-triangular arrangement.

	$\bar{C}_d$	$C'_l$	$St$
$Re = 50$			
Mittal (2005)	1.416	0.035	0.123
Qu <i>et al.</i> (2013)	1.397	0.039	0.124
Present	1.427	0.039	0.123
$Re = 100$			
Williamson (1989)	—	—	0.164
Park, Kwon & Choi (1998)	1.33	0.235	0.165
Li <i>et al.</i> (2009)	1.336	—	0.164
Present	1.337	0.230	0.163
$Re = 150$			
Posdziech & Grundmann (2001)	1.314	0.356	0.184
Qu <i>et al.</i> (2013)	1.306	0.355	0.184
Present	1.316	0.363	0.181
$Re = 200$			
Mittal (2005)	1.327	0.489	0.196
Qu <i>et al.</i> (2013)	1.32	0.457	0.196
Present	1.324	0.474	0.194

TABLE 1. Comparison of flow past an isolated circular cylinder at  $Re = 50$ – $200$ .

	$\bar{C}_d$	$\bar{C}_l$	$C'_l$
Kang (2003) ( $B = 0.005$ )	1.43	0.178	0.191
Lee <i>et al.</i> (2009) ( $B = 0.02$ )	1.423	0.178	0.169
Bao, Zhou & Tu (2013) ( $B = 0.005$ )	1.431	0.177	0.211
Present ( $B = 0.005$ )	1.424	0.176	0.191

TABLE 2. Comparison of flow past two side-by-side cylinders at  $L/D = 2.5$  and  $Re = 100$ .

	$\bar{C}_{d1}$	$C'_{d1}$	$\bar{C}_{l1}$	$C'_{l1}$	$\bar{C}_{d2}$	$C'_{d2}$	$\bar{C}_{l2}$	$C'_{l2}$
Bao <i>et al.</i> (2010) ( $B = 0.01$ )	1.05	0.001	0	0.0175	1.26	0.0167	-0.06	0.201
Zheng <i>et al.</i> (2016) ( $B = 0.045$ )	1.23	0.0288	0	-0.002	1.53	0.0214	-0.087	0.335
Present ( $B = 0.005$ )	1.03	0.0014	0	0.0173	1.23	0.0169	-0.059	0.182
Present ( $B = 0.0025$ )	1.03	0.0015	0	0.0172	1.23	0.0168	-0.059	0.181

TABLE 3. Comparison of flow past three circular cylinders in an equilateral-triangular arrangement with  $L/D = 3.0$  and  $Re = 100$ .

$\Delta tU/D$	$\bar{C}_{d1}$	$C'_{d1}$	$\bar{C}_{l1}$	$C'_{l1}$	$\bar{C}_{d2}$	$C'_{d2}$	$\bar{C}_{l2}$	$C'_{l2}$	$St$
0.001	1.03	0.0014	0	0.0173	1.23	0.0163	-0.059	0.182	0.137
0.002	1.03	0.0014	0	0.0173	1.23	0.0169	-0.059	0.182	0.137
0.004	1.03	0.0014	0	0.0173	1.23	0.0166	-0.059	0.181	0.137

TABLE 4. Flow past three circular cylinders in an equilateral-triangular arrangement at  $L/D = 3.0$  and  $Re = 100$  with different  $\Delta tU/D$ .

range of  $Re$  examined. The present results in table 2 agree well with those in Kang (2003) and Bao *et al.* (2013) which have the same blockage ratio  $B (= D/H = 0.005)$ , where  $H$  is the transverse width of the computational domain. The largest discrepancy ( $\sim 11.5\%$ ) is observed for  $C'_l$  between the present and that of Lee *et al.* (2009). This discrepancy is attributed to the large  $B (= 0.02)$  in Lee *et al.* (2009). Finally, for the three cylinders, the present results with  $B = 0.005$  are in good agreement with those in Bao *et al.* (2010) with  $B = 0.01$ . However, significant discrepancies are observed between the present results and those of Zheng *et al.* (2016) where  $B = 0.045$  is much larger than that ( $= 0.005$ ) in the present computation. It is found that the difference in the present results between  $B = 0.0025$  and  $0.005$  is negligible, confirming that  $B = 0.005$  is small enough for the computation of the three-cylinder flow. Even the total blockage ratio  $B' = 3D/H = 0.015$ , considering the blocking effects of three cylinders, still satisfies the criterion ( $\sim 0.01-0.02$ ) suggested in Sen, Mittal & Biswas (2009) and Chen *et al.* (2015a). Therefore,  $B = 0.005$  is adopted for the subsequent simulations.

The adopted non-dimensional time step size is checked in the case of flow past three cylinders in an equilateral-triangular arrangement at  $L/D = 3.0$  and  $Re = 100$ . Table 4 shows a very small marginal difference between the results for three different time steps  $\Delta tU/D = 0.001, 0.002$  and  $0.004$ . Hereafter the non-dimensional time step size of  $0.002$  is adopted.

### 3. The effects of the spacing ratio

In this section, the flow structures, fluid forces acting on the three cylinders and spectral features of the lift forces are presented for the range of  $L/D = 1.0-6.0$  at  $Re = 100$ . A minimum interval of  $\Delta L/D = 0.1$  is applied to understand how the flow structures and hydrodynamic forces are sensitive to  $L/D$ . Based on the vortex-shedding timing between the two downstream cylinders, the interaction of the three cylinders and the evolution of the shear layers, six flow regimes are classified. The flow structures are named single bluff-body flow (SB,  $1.0 \leq L/D \leq 1.4$ ), deflected gap flow (DF,  $1.4 < L/D \leq 1.9$ ), flip-flopping flow (FF,  $1.9 < L/D \leq 2.5$ ), anti-phase flow

(AP,  $2.5 < L/D \leq 2.8$  and  $3.4 < L/D \leq 4.1$ ), in-phase flow (IP,  $2.8 < L/D \leq 3.4$  and  $4.1 < L/D \leq 4.5$ ) and fully developed in-phase co-shedding flow (IC,  $4.5 < L/D \leq 6.0$ ). Details of these flow regimes are given in the following subsections.

### 3.1. Flow structures

#### 3.1.1. Single bluff-body flow ( $1.0 \leq L/D \leq 1.4$ )

When  $L/D$  is small, the shear layers of the upstream cylinder (Cylinder 1) reattach on the free-stream-side surface of the downstream cylinders (Cylinders 2 and 3) and enclose Cylinders 2 and 3. The three cylinders behave like a single bluff body (figure 2*a*). The vortex shedding occurs from the free-stream sides of the downstream cylinders and the vortices are arranged in a similar fashion to the typical Kármán vortex street. Several cylinder diameters downstream, the vortices appear in two parallel rows. With an increase in  $L/D$ , the upstream-cylinder-generated shear layers reattach on the front surface of the downstream cylinders, which allows a small share of the shear layers to go through the gap between the cylinders to form a symmetric gap flow. The intensity of the gap flow increases with the increasing  $L/D$ . Gradually, two shear layers are developed on the gap-side surface of the downstream cylinders.

At  $L/D = 1.1$ , the gap flow is weak and no shear layer is observed between the two downstream cylinders (see figure 2*b* that is a zoomed-in view of the flow around cylinders in figure 2*a*). When  $L/D \geq 1.2$ , two shear layers are alternately generated from the inner sides of the downstream cylinders and swerve toward the base of the cylinder, following the shedding from the free-stream side, as shown in figure 2*c*). A small share of the growing vortex from the other free-stream side merges with the inner shear layer. With further increasing  $L/D$ , the flow through the gap enhances, the inner shear layers grow and thicken. As shown in figure 2*e*), the normalized time-mean streamwise velocity shows a parabolic profile in the gap  $G$  and is perfectly symmetric with respect to the centreline ( $y/D = 0$ ). The velocity at the gap centreline increases with  $L/D$ . A large recirculation bubble forms behind the cylinders because of the shedding from the free-stream sides (figure 2*d*). Figure 2*f*) shows the non-dimensional streamwise distance ( $L_b/D$ ) of the centre of the recirculation bubbles measured from the centre of the downstream cylinders. It can be seen that  $L_b/D$  exponentially increases with increasing  $L/D$ .

In this flow regime, variations in instantaneous drag and lift coefficients are regular and periodic with the same dominant frequency, as shown in figures 2*g*) and 2*h*), which supports the findings that three cylinders behave like a single bluff body. As the vortices are only shed from the free-stream sides of the downstream cylinders, the time-mean drag coefficients are much larger for the downstream cylinders than the upstream (figure 2*g*). Similarly, the lift coefficients of the downstream cylinders show larger amplitudes, due to the same reason, see figure 2*g*). The fluctuations of the lift for the three cylinders are close to in phase, again suggesting that the three cylinders act as a single bluff body. As shown in figure 2*h*), the non-dimensional vortex shedding frequencies of the three cylinders are the same,  $St = f_i D/U = 0.099$  at  $L/D = 1.2$ , obviously lower than  $St = 0.164$  for the flow past an isolated circular cylinder at  $Re = 100$ . Here,  $f_i$  denotes the dominant frequencies of the lift force fluctuation. Note that a second harmonic frequency,  $St = 0.198$ , emerges for the downstream cylinders, caused by the interactions of the upstream-cylinder-generated shear layers with the downstream cylinder. Alam (2014) for two tandem cylinders identified a second harmonic frequency in the lift fluctuations when the upstream-cylinder shear layers reattach on the surface of the downstream cylinder. The presence of the second harmonic frequency for the three-cylinder case is consistent with Alam's observation.

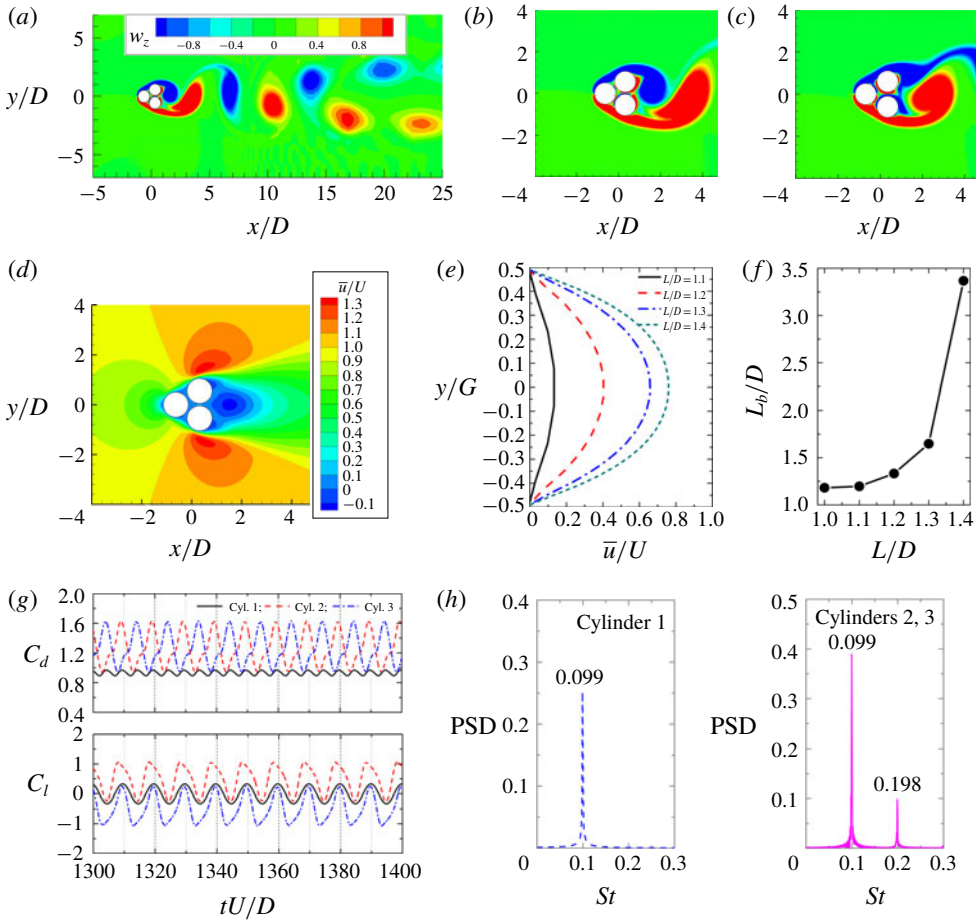


FIGURE 2. Flow and force characteristics at  $Re = 100$  ( $L/D = 1.1$  and  $1.2$ ). (a,b) Vorticity contours ( $L/D = 1.1$ ) where (b) represents a zoom-in view of (a), (c) vorticity contours ( $L/D = 1.2$ ), (d) time-averaged streamwise velocity field ( $L/D = 1.1$ ), (e) non-dimensional streamwise velocity profiles in the gap of two downstream cylinders, (f) non-dimensional streamwise length between the bubble centres and the centres of two downstream cylinders, (g) time histories of the drag and lift coefficients ( $L/D = 1.2$ ) and (h) power spectral density (PSD) of the lift coefficients ( $L/D = 1.2$ ). The legends in (a) and (d) apply to the contours of the vorticity and the time-averaged streamwise velocity, respectively, in this figure and those thereafter.

### 3.1.2. Deflected gap flow ( $1.4 < L/D \leq 1.9$ )

With a further increase in  $L/D$ , the gap flow may deflect to one of the downstream cylinders and generate the deflected gap flow pattern (figure 3a–c). The gap flow between the two downstream cylinders deflects toward the upper one and creates a narrow wake behind it. Three sequential instantaneous vorticity snapshots (a–c) in a half of the vortex-shedding period are presented where Cylinder 2 has the lowest and highest lift at instants a and c, respectively, with instant b corresponding to the mean lift. No spontaneous switch of the gap flow was identified. The gap flow was stably deflected toward the upper or the lower downstream cylinder at

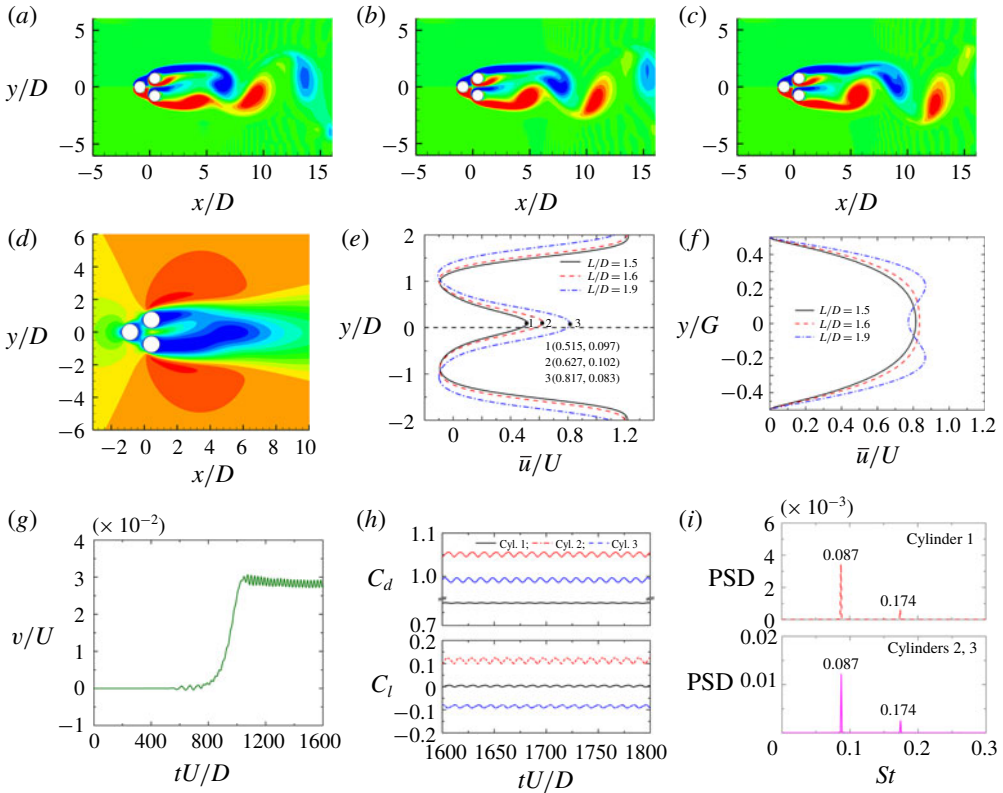


FIGURE 3. Flow and force characteristics at  $L/D = 1.5$ – $1.9$ . (a–c) Vorticity contours ( $L/D = 1.5$ ) corresponding to the lowest, median and highest lift of Cylinder 2, respectively. (d) The time-averaged streamwise velocity field ( $L/D = 1.5$ ). (e) Time-averaged non-dimensional streamwise velocity at  $1D$  behind two downstream cylinders along  $y/D = -2 \sim +2$ . (f) The time-averaged streamwise velocity profiles in the gap between two downstream cylinders. (g) Time history of the non-dimensional transverse velocity at the midpoint of two downstream cylinders ( $L/D = 1.6$ ). (h) Time histories of the drag and lift coefficients ( $L/D = 1.5$ ). (i) Spectra of the lift coefficients ( $L/D = 1.5$ ).

different runs of the simulations. For two side-by-side cylinders, some experimental and numerical investigations showed the switch of the gap flow (Bearman & Wadcock 1973; Kim & Durbin 1988; Alam *et al.* 2003a) but some did not (Williamson 1985; Sumner *et al.* 1999). Presently, the presence of the upstream cylinder may restrict the switch of the deflected gap flow. The flow through the gap is still weak, the gap shear layers are therefore short in the streamwise length and do not roll up appreciably. The vortices are alternately shed from the free-stream sides of the downstream cylinders, with the vortex formation length significantly longer than that for  $L/D = 1.1$  or  $1.2$  (figure 2a–c). The longer formation implies that the gap flow effectively acts as a base-bleed flow. Due to the presence of the upstream cylinder and the small gap between the downstream cylinders, the flow through the gap between the downstream cylinders is still weak, and the three cylinders act as a single combined bluff body. The gap flow provides some of the entrainment required by the free shear layers and the vortices. The entrainment within the separated near-wake region is thus decreased, and the base pressure increases. Wood (1967) examined the effect of base bleed

(low-momentum fluid injected through the rear stagnation point) on vortex shedding and wake structure. He found that the base bleed displaces the shear layer rolling away from the cylinder and increases the pressure on the rear surface. The base bleed is only effective if low-momentum fluid is fed into the wake. The same opinion was also shared by Bearman & Wadcock (1973) for two side-by-side circular cylinders at small gap spacing. Figure 3(d) shows the time-averaged streamwise velocity at  $L/D = 1.5$ . Two recirculation bubbles form, one is short, behind Cylinder 2 that corresponds to a larger drag; and the other is long, behind Cylinder 3 experiencing lower drag (figure 3d,h). This is similar to the biased gap flow pattern observed for two side-by-side cylinders (Alam *et al.* 2003a; Kang 2003; Supradeepan & Roy 2014), where the cylinder with a narrow wake has a higher drag and the other with a wide wake has a lower drag.

Figure 3(e) shows the streamwise velocity profiles at  $1D$  behind the downstream cylinders. The maximum gap velocity increases with increasing  $L/D$ . However, the transverse shift of the maximum from the wake centreline ( $y/D = 0$ ) is  $y/D = 0.097$ ,  $0.102$  and  $0.083$  for  $L/D = 1.5$ ,  $1.6$  and  $1.9$ , respectively, indicating the deflection of the gap flow is the most significant at  $L/D = 1.6$ . After the critical  $L/D = 1.6$ , the gap flow tends to be parallel to the free-stream lines. One of the reasons is that, with the increase of  $L/D$ , the gap flow becomes thicker and gains sufficient momentum to become straight. Figure 3(f) shows the gap flow streamwise velocity variation with  $L/D$ . While the profile of the mean streamwise velocity is parabolic, with a flattened peak near  $y/G = 0$  for  $L/D = 1.5$  and  $1.6$ , it has two peaks for  $L/D = 1.9$ . In the former case, the shear layers separated from the upstream cylinder largely follow the free-stream-side shear layers of the downstream cylinder. On the other hand, in the latter case, those go into the gap between the downstream cylinders, leading to the formation of two peaks.

As shown in figure 3(g), once the gap flow deflects to one cylinder, it is captured by the low-pressure region behind the cylinder and does not sway to the other cylinder. Figure 3(h,i) presents the force characteristics of the three cylinders at  $L/D = 1.5$ . The mean drag coefficient is larger for the downstream cylinders than the upstream cylinder. The mean drag coefficient of Cylinder 2, toward which the gap flow deflects, is larger than that of Cylinder 3. The fluctuation in the lift coefficient of Cylinder 1 is rather small, compared with those of Cylinders 2 and 3. The mean lift on Cylinder 1 is zero while Cylinder 2 has a larger absolute value than Cylinder 3, which is due to the deflection of the gap flow. As indicated by figure 3(i), the dominant frequencies for the three cylinders are the same ( $St = 0.087$ ). Similar to the single bluff-body flow, a superharmonic frequency ( $St = 0.174$ ) emerges in the spectra of the lift forces for the three cylinders. It should be pointed out that Cylinder 3 has the same frequencies as Cylinder 2, although the gap flow is deflected toward Cylinder 2, again suggesting the dominant shedding from the free-stream sides.

### 3.1.3. Flip-flopping gap flow ( $1.9 < L/D \leq 2.5$ )

For  $1.9 < L/D \leq 2.5$ , the shear layers separated from the upstream cylinder are fully trapped and squeezed by the downstream cylinders (figure 4a–c). More fluid thus goes through the gap, making the gap-side shear layers stronger. The gap flow changes its direction occasionally and irregularly. This wake flow was named as flip-flopping (FF) by Bearman & Wadcock (1973) in the experimental study of the flow around two side-by-side circular cylinders. The three instants in figure 4(a–c) show the process of the gap flow direction changing from Cylinder 2 to Cylinder 3. These instants are also marked in the time histories of the drag and lift coefficients in figure 4(g). In

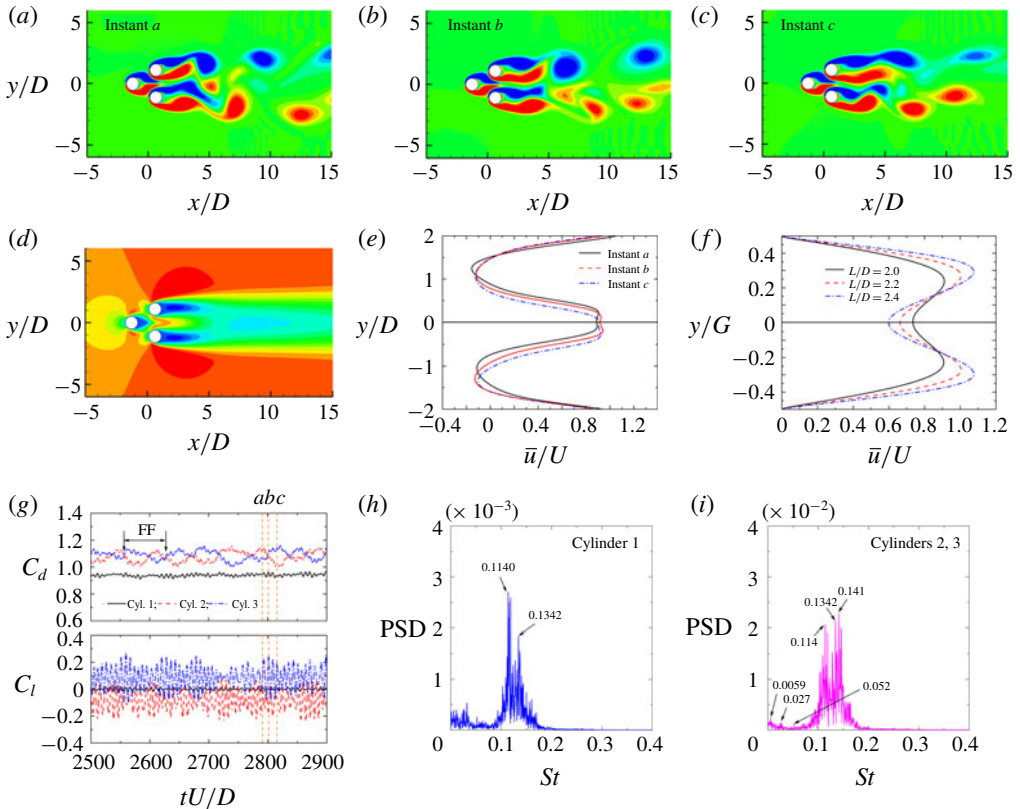


FIGURE 4. Flow and force characteristics at  $L/D = 2.2$ . (a–c) Correspond to the upward deflected, parallel and downward deflected gap flow. (d) The time-averaged streamwise velocity. (e) The time-averaged streamwise velocity profiles at  $1D$  behind the centres of two downstream cylinders. (f) The time-averaged streamwise velocity profiles in the gap of two downstream cylinders. (g) Time histories of the drag and lift coefficients. (h) Spectra of the lift coefficients.

figure 4(a), the gap flow deflects toward Cylinder 2, giving rise to the drag coefficient of Cylinder 2 being larger than that of Cylinder 3. When the gap flow changes its direction from Cylinder 2 to 3 or *vice versa*, an intermediate state exists where the gap flow is parallel to the free-stream flow (see figure 4b), generating equal mean drag coefficients of the two downstream cylinders. In figure 4(c), the gap flow deflects toward Cylinder 3.

Figure 4(d) shows the time-averaged streamwise velocity field; it is symmetric about  $y/D = 0$ . Figure 4(e) shows the instantaneous streamwise velocity profiles at  $1D$  behind the downstream cylinders along the  $y$ -axis at instants *a*, *b* and *c*. At instant *a*, the maximum velocity is larger on the upper side than on the lower side, confirming the gap flow deflection toward Cylinder 2. The whole flow profile is shifted up. On the other hand, the profile is downshifted at instant *c* while symmetric at instant *b*.

As shown in figure 4(f), with the increase of  $L/D$ , the upstream shear layers enter further downstream in the gap. The maximum time-averaged streamwise velocity surpasses the free-stream flow velocity. Here, the upstream-cylinder shear layers are not reattached on the downstream cylinders, but squeezed toward the centreline.

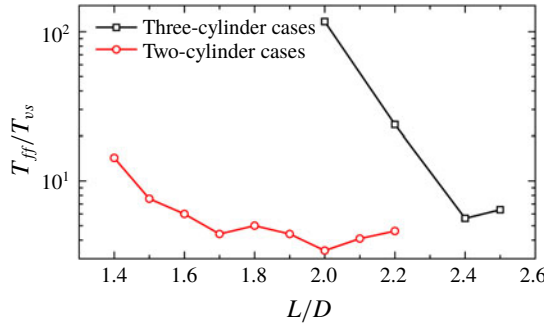


FIGURE 5. The ratios of flip-over time scale ( $T_{ff}$ ) to the vortex-shedding period ( $T_{vs}$ ) in the equilateral-triangular and the side-by-side configurations.

Strong shear layers, comparable to the free-stream-side shear layers, form on the inner sides of the downstream cylinders (figure 4*a-c*), leading to the formation of two peaks in the velocity profile (figure 4*f*). The significantly enlarged shearing rate intensifies the instability of the gap flow. As a result, the stably deflected gap flow in the DF regime transforms into the FF one.

However, the FF flow pattern of three cylinders in the triangular arrangement shows some differences from that for two side-by-side cylinders due to the presence of the upstream cylinder. Time histories of the drag and lift coefficients of the three cylinders clearly illustrate a low frequency variation in the drag and lift coefficients (figure 4*g*). Figure 4(*h*) shows the amplitude spectra of the three cylinders. Three dominant shedding frequencies ( $St = 0.114, 0.1342$  and  $0.141$ ) are discernible for Cylinders 2 and 3. The same is reflected for Cylinder 1, albeit that the energies at the peaks are small and the peak at  $St = 0.141$  disappears. For the downstream cylinders, besides the comparable peaks at  $St = 0.114, 0.1342$  and  $0.141$ , a lower frequency is observed at  $St = 0.0059$  which is related to the flip-over of the gap flow direction. The ratio of the dominant frequency to the lower one can be used to determine the average flip-over time normalized by the vortex-shedding period. For instance, at  $L/D = 2.2$ , the average flip-over time equals to  $0.141/0.059 \approx 24$  cycles of vortex shedding. Note that the FF flow is highly irregular and aperiodic, and the flip-over time varies with a large deviation. Here, we used the predominant high and low frequencies to give a reasonable estimation of the flip-flopping period. However, this estimation cannot be directly used for the comparison with a particular FF cycle due to the reason above.

In order to discuss the flip-over time for different configurations, figure 5 shows the ratios of the flip-over time scale ( $T_{ff}$ ) to the vortex-shedding period ( $T_{vs}$ ) for the triangular configuration (TC) and the side-by-side configuration (SC) at different  $L/D$ . It is seen that the ratio for the TC is at least one order of magnitude larger than that for the SC, with the exceptions at  $L/D = 2.4$  and  $2.5$  where the two ratios are comparable. Moreover, FF exists in the range of  $2.0 \leq L/D \leq 2.5$  for TC and  $1.4 \leq L/D \leq 2.2$  for SC (Kang 2003; Chen *et al.* 2015*b*). This discrepancy can be attributed to the shielding effect of the upstream cylinder and the counteraction between the shear layers of the upstream and downstream cylinders, which attenuates the gap-side shear layers of the downstream cylinders.

### 3.1.4. Anti-phase flow ( $2.5 < L/D \leq 2.8$ ; $3.4 < L/D \leq 4.1$ )

Anti-phase flow is referred to as the case where the fluctuations in lift of the two downstream cylinders are  $180^\circ$  out of phase. This happens when the vortices

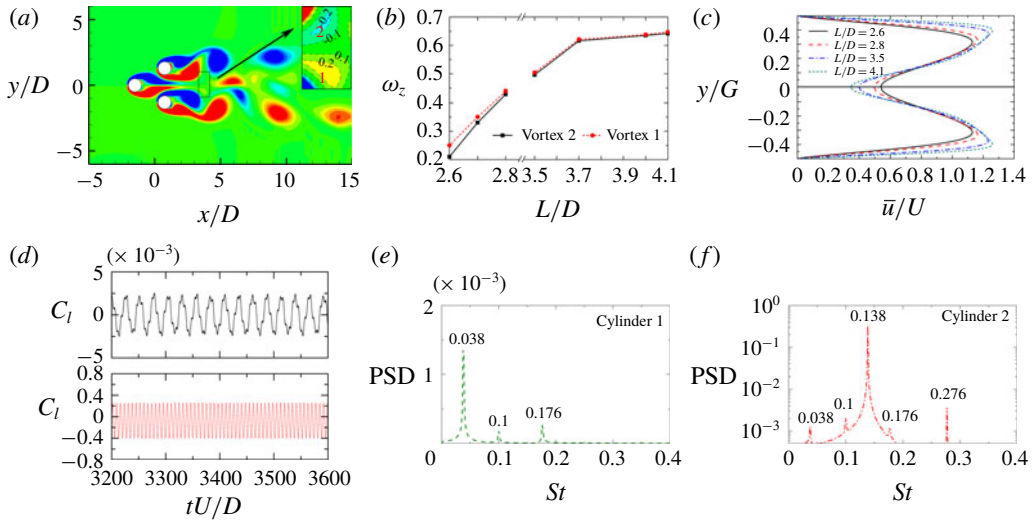


FIGURE 6. Flow and force characteristics in the anti-phase regime. (a) Vorticity contours at  $L/D=2.6$ . Vortices 1 and 2 marked in (a) are shed from the upstream cylinder. (b) The maximum  $z$ -vorticity (absolute value) of the vortex pair shed from the upstream cylinder. (c) The time-averaged gap flow streamwise velocity profiles at  $L/D=2.6$ –4.1. (d) Time histories of the lift coefficients at  $L/D=2.7$ . (e) Lift spectrum of Cylinder 1. (f) Lift spectrum of Cylinder 2.

are simultaneously shed from the free-stream/gap sides of the downstream cylinders, appearing symmetric about the wake centreline. As shown in figure 6(a), the vortices shed from the gap side of the downstream cylinders are weaker than those from the free-stream sides and vanish after several vortex-shedding lengths. The shear layers of the upstream cylinder pass through the gap and roll-up into weak vortices downstream (see the inset). During the vortex shedding from the free-stream sides of the downstream cylinders, the gap-side shear layers are thin and short, leaving more room for the upstream shear layers to enter into the gap. Oppositely, during the vortex shedding from the gap sides, the two gap-side shear layers, becoming thick and long, move toward each other, which cuts down the vorticity supplement from the extruded upstream shear layers and thus generate two weak vortices, as shown in the inset in figure 6(a). These vortices have the same shedding frequency as those from the two downstream shear layers. With the increase of  $L/D$ , the intensity of the vortices shed from the upstream cylinder increases. As shown in figure 6(b), the maximum vorticity  $\omega_z$ , defined in a non-dimensional form as  $\omega_z = (\partial v / \partial x - \partial u / \partial y)(D/U)$ , increases from 0.21–0.25 at  $L/D=2.6$  to 0.642–0.647 at  $L/D=4.1$ .

With increasing  $L/D$ , the change from regimes FF to AP allows more fluid to enter into the gap between the two downstream cylinders. No interaction of the gap-side vortices exists due to the segregating effects of the upstream shear layers. Therefore, the flip-flopping flow transmutes to the anti-phase flow. Figure 6(c) shows the gap flow streamwise velocity profiles at different  $L/D$ . Although the profiles are similar to each other, with increasing  $L/D$  the velocity at the gap centre decreases and that in the gap shear layers (peak) grows, indicating that the upstream shear layers enter further into the gap.

Figure 6(d–f) shows time histories and power spectra of the lift coefficient. As the lift and spectra are the same for the two downstream cylinders, only the results for

Cylinder 2 are shown. Different from a pure periodic AP flow occurring for two side-by-side cylinders (Mizushima & Ino 2008; Carini, Giannetti & Auteri 2014a), the AP flow for three equilaterally arranged cylinders features weak fluctuations in lift of the upstream cylinder (figure 6d) and asymmetric gap vortex shedding (figure 6a). This unique feature emerges due to the presence of the upstream cylinder that introduces an instability into the gap flow. An observation on the lift history of the upstream cylinder revealed that the pure periodic AP flow, without fluctuations, occurs at the early stage of the computation ( $tU/D < 500$ ), i.e. when the flow develops. The lift fluctuation begins at  $tU/D \approx 500$  and statistically converges at  $tU/D > 2500$ . As shown in figure 6(e-f), the dominant frequency in the lift of the upstream cylinder is  $St = 0.038$  and that of the downstream cylinders is  $St = 0.138$ . This spectral feature is an analogy to what is observed for the early FF regime of two side-by-side cylinders (Carini *et al.* 2014b; Carini, Auteri & Giannetti 2015). Other peaks emerging in the spectra are due to the nonlinear interaction of the two frequencies, e.g.  $St = 0.10 = 0.138 - 0.038$  and  $St = 0.176 = 0.138 + 0.038$ .

The low-frequency lift at  $St = 0.038$  is related to the asymmetry of the vortex shedding. For example, with the increase of  $L/D$ , the vorticity difference of the vortex pair shed from the upstream shear layers decreases significantly, from 16% at  $L/D = 2.6$  to 0.8% at  $L/D = 4.1$  (see figure 6b), indicating that the symmetry of the wake is gradually re-established.

### 3.1.5. In-phase flow ( $2.8 < L/D \leq 3.4$ ; $4.1 < L/D \leq 4.5$ )

Figure 7(a,b) shows the vorticity contours at  $L/D = 3.2$  and  $4.5$  belonging to the separated in-phase flow ranges  $2.8 < L/D \leq 3.4$  and  $4.1 < L/D \leq 4.5$ , respectively. Due to a larger spacing ratio, the vortices shed from the upstream cylinder in the second in-phase range are stronger than that in the first in-phase range. The vortex shedding from the downstream cylinders occurs in an in-phase fashion (figure 7a,b). See also the lift variations of Cylinders 2 and 3 (figure 7e). In other words, the two gap shear layers of Cylinders 2 and 3 are anti-phase in view of their vortex shedding. The two shear layers of the upstream cylinder perceptibly swing in the gap, following the vortex shedding from the gap shear layers. The vortices from the upstream-cylinder shear layers are stretched and interact with the opposite-sign vortices from the gap-side shear layers. The interactions result in cancellations of vorticities from the gap-side shear layers, engendering a rapid decay of vortices from the gap. Two rows of vortices from the free-stream sides thus survive downstream.

As shown in figure 7(c), the time-averaged vorticity field is symmetric about  $y/D = 0$ . Figure 7(d) shows streamwise velocity profiles for the gap flow. In the first range ( $2.8 < L/D \leq 3.4$ ), the value of  $\bar{u}/U$  in the trough of the profile decreases with  $L/D$ . However, this increases with  $L/D$  in the second range ( $4.1 < L/D \leq 4.5$ ). This is because, in the first range, the low-momentum upstream shear layers gradually enter into the expanding gap, reducing the trough value. However, in the second range the swing of the upstream-cylinder shear layers causes an enhanced momentum passing through the gap with enhanced fluid mixing. For the same reason, the peak value is larger for the second range than for the first range, with the boundary layer thickness thinning for the second range (i.e. a rapid growth of  $\bar{u}/U$  with  $y/G$  moving from the cylinder surface).

Figure 7(e,f) shows time histories of fluid forces and amplitude spectra of the lift coefficient at  $L/D = 4.5$ . It can be seen that the r.m.s. lift and drag coefficients of the upstream cylinder are much lower than those of the downstream cylinders. In addition, the mean drag coefficient is also larger for a downstream cylinder than for the upstream cylinder. The vortex-shedding frequencies of the three cylinders are identical, i.e.  $St = 0.146$ .

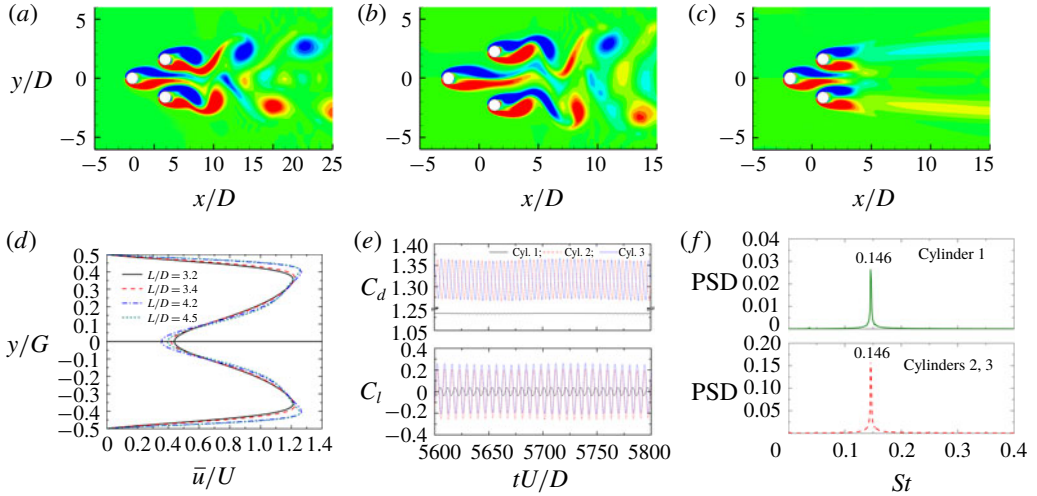


FIGURE 7. Instantaneous vorticity fields at  $L/D = 3.2$  (a) and  $4.5$  (b). (c) Time-averaged vorticity field at  $L/D = 3.2$ . (d) Time-averaged streamwise velocity profiles in the gap of two downstream cylinders. (e) Time histories of the drag and lift coefficients at  $L/D = 4.5$ . (f) Lift spectra of three cylinders at  $L/D = 4.5$ .

### 3.1.6. Fully developed in-phase co-shedding flow ( $4.5 < L/D \leq 6.0$ )

In this pattern, fully developed vortices shed from the upstream cylinder in the space surrounded by the cylinders, pairing with the vortices shed from the downstream cylinders, see figure 8(a,b). Indeed, the arrival of upstream-cylinder-generated vortices in the gap between the downstream cylinders triggers the vortex shedding from the corresponding gap sides of the downstream cylinders. The vortex shedding from the two downstream cylinders is thus always in phase, and the phase lag between the vortex shedding from the upstream and downstream cylinders is dependent on  $L/D$  (Alam & Zhou 2007; Alam 2016). To elucidate the triggering and vortex evolution processes, the vortices in the wake have been numbered as 1A1, 2B2, 3A1, etc. in figure 8(a). Here A and B indicate the cylinder sides (or vortex sign), A for negative vortex (upper side) and B for positive vortex (lower side). The number before the vortex letter indicates the cylinder from which the vortex originated while the number after the vortex letter indicates the vortex-shedding sequence. For example, 3B1 means the vortex is from Cylinder 3, shed from the lower side (positive vortex). Vortices 1A2 and 2B1 are in the process of pairing whilst vortex 1B2 has paired with 3A2 (Williamson 1985). The paired vortices 1B2 and 3A2 separate from each other during their downstream evolution, as can be seen from the positions of their sibling vortices 1B3 and 3A3. An observation of the evolution of the vortices in the wake suggests that the vortices from the upstream cylinder decay faster than those from the downstream cylinders, see  $(1A3 \rightarrow 1A4 \rightarrow 1A5)/(1B2 \rightarrow 1B3 \rightarrow 1B4)$  and  $(2A2 \rightarrow 2A3 \rightarrow 2A4)/(2B2 \rightarrow 2B3 \rightarrow 2B4)$  or  $(3A2 \rightarrow 3A3 \rightarrow 3A4)/(3B2 \rightarrow 3B3 \rightarrow 3B4)$ . The vortices from the upper and lower sides of the upstream cylinder move downward and upward, respectively. As 1B2 lies between clockwise vortex 2A2 and anticlockwise vortex 2B1, the upward flow generated between 2A2 and 2B1 causes the separation of 1B2 from 3A2, taking 1B2 to the upper side. At  $L/D = 5.0$  (figure 8b), the vortex evolution scenario is the same except that all gap vortices get biased downward during their convection. This is can be attributed to

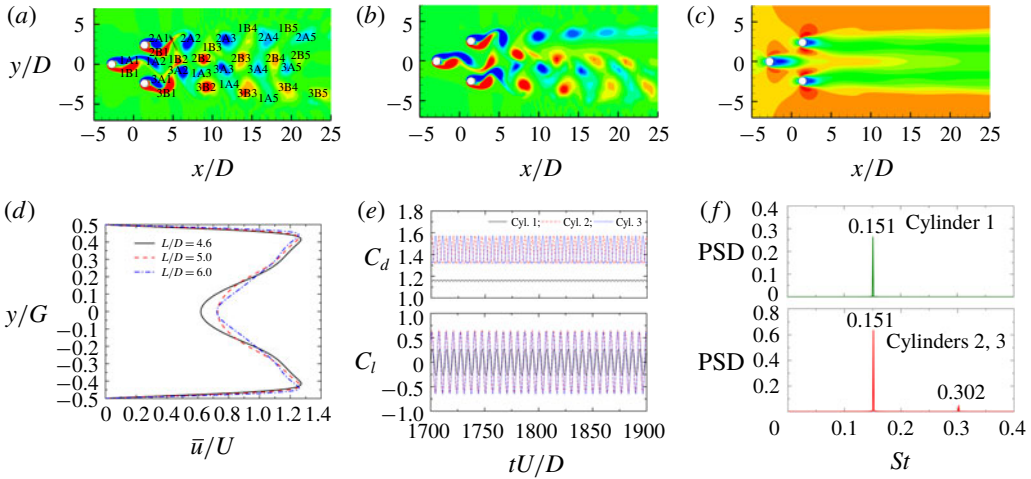


FIGURE 8. Instantaneous vorticity fields at  $L/D=4.8$  (a) and  $5.0$  (b). (c) Time-averaged streamwise velocity field at  $L/D=4.8$ . (d) Time-averaged streamwise velocity profiles in the gap of two downstream cylinders. (e) Time histories of the drag and lift coefficients and (f) lift spectra of three cylinders at  $L/D=4.8$ . The arrow in (a) indicates the upward flow generated between 2A2 and 2B1.

the vortex-shedding phase lag ( $\phi_{12}$  and  $\phi_{13}$ ) between the upstream cylinder and the downstream cylinders. It will be shown later that  $\phi_{12}$  is slightly (approximately 9%) larger than  $\phi_{13}$ , indicating that the vortices shed from the upper and lower sides of the upstream cylinder undergo different interactions with the gap vortices of the downstream cylinders. Figure 8(c) shows the time-mean streamwise velocity field. The bubble length behind the upstream cylinder is larger than that of a downstream cylinder. Figure 8(d) shows the gap flow streamwise velocity. The value of  $\bar{u}/U$  at the trough ( $y/G=0$ ) generally increases with increasing  $L/D$ , much smaller for  $L/D=4.6$ . When  $L/D \geq 5.0$ , the streamwise velocity profiles are almost the same and the vortex shedding from the upstream cylinder approaches that of an isolated cylinder.

Figure 8(e,f) shows time histories of fluid forces and amplitude spectra of the lift coefficients. The r.m.s. lift and drag coefficients of the downstream cylinders are larger than those of the upstream cylinder, while the mean drag coefficients are the same for the three cylinders. As indicated by figure 8(f), the three cylinders have the same dominant lift frequency, i.e.  $St=0.151$  at  $L/D=4.8$ . In addition, a superharmonic frequency, which is related to the interaction of the upstream-cylinder-generated vortices with the gap-side vortices from the downstream cylinder, is observed in the spectra of the downstream cylinders.

### 3.2. Hydrodynamic forces, Strouhal number, phase lag and gap flow

#### 3.2.1. Drag coefficient

Figure 9(a) displays the variations in  $\bar{C}_d$  of the three cylinders with  $L/D$ . In the range  $L/D=1.0-1.4$ ,  $\bar{C}_d$  values of the downstream cylinders show a first increasing then decreasing trend with the maximum value ( $\bar{C}_d=1.26$ ) occurring at  $L/D=1.2$  followed by a decrease. In the deflected pattern region ( $L/D=1.5-1.9$ ), the values of  $\bar{C}_d$  of the downstream cylinders are unequal because of the stably biased gap flow. The

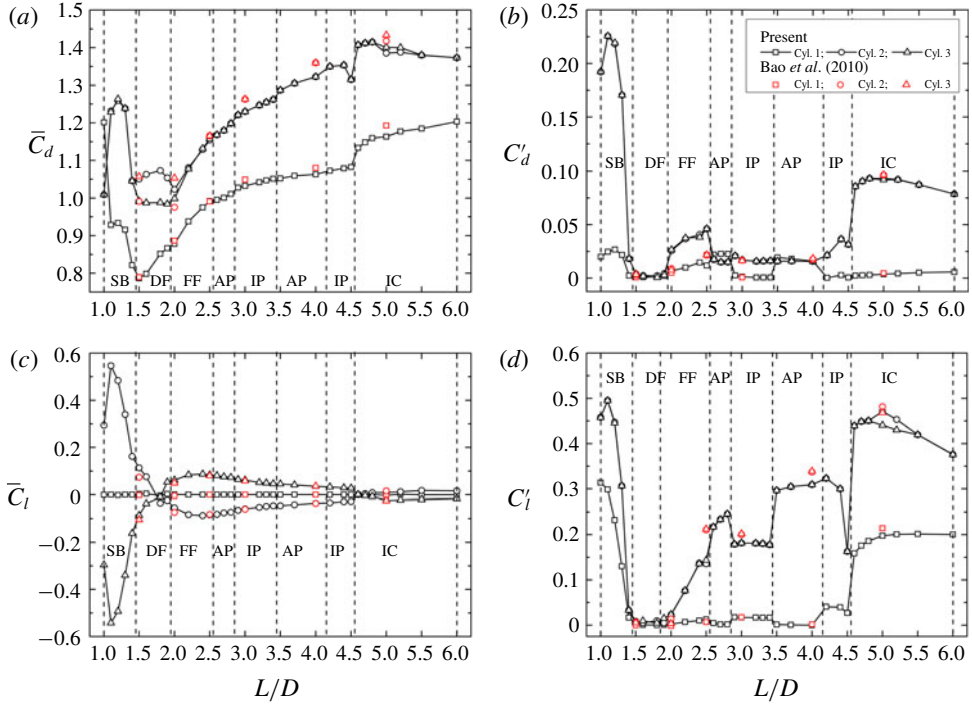


FIGURE 9. Hydrodynamic forces of three cylinders. The wake patterns are separated by the dashed line. SB, single bluff-body flow; DF, deflected flow; FF, flip-flopping flow; AP, anti-phase flow; IP, in-phase flow; IC, fully developed in-phase co-shedding flow.

deflection angle can be inferred from the difference between the values of the mean drag coefficients of the downstream cylinders. When the gap flow deflection angle is zero, the two cylinders are expected to have an equal drag. A larger deflection of the gap flow may induce a larger difference in the drag forces between the cylinders (Alam *et al.* 2003a; Akilli, Akar & Karakus 2004; Alam, Zhou & Wang 2011; Dadmarzi *et al.* 2018). It should be mentioned here that, in figure 9, only the results with the gap flow deflecting toward the upper cylinder are given. As  $L/D$  increases to 2.0–2.5, the wake flow turns into the flip-flopping pattern. The  $\bar{C}_d$  values of the downstream cylinders again become equal if the average is taken over a sufficiently long period (e.g. greater than 100 switching periods) time (Kang 2003; Carini *et al.* 2014b). In this study, limited by the computing resources, equal  $\bar{C}_d$  values are not achieved for  $L/D = 2.0$  because the FF switching period was long, two orders of magnitude longer than the vortex-shedding period. However, when  $L/D \geq 2.2$ , the FF switching time was short, less than approximately ten times the vortex-shedding period. An identical  $\bar{C}_d$  is achieved for the downstream cylinders. In the region of  $2.5 \leq L/D \leq 4.5$ , encompassing the anti-phase and in-phase patterns, the  $\bar{C}_d$  values of the downstream cylinders monotonically increase with  $L/D$ . The increase is attributed to the increase in vorticities in the shear layers and to the shift of the shear layer roll-up to the cylinder base. The  $\bar{C}_d$  of a downstream cylinder attains its maximum of 1.41 at  $L/D = 4.6$ , followed by a gradual decrease.

For the upstream cylinder,  $\bar{C}_d$  is maximum at the smallest  $L/D (= 1.0)$ . This is the only  $L/D$  at which the upstream cylinder has a larger  $\bar{C}_d$  than the two downstream

cylinders. The value of  $\bar{C}_d$  in the SB regime declines with a small attenuation around  $L/D=1.2$ . The value of  $\bar{C}_d$  has a minimum of 0.79 at the border between the SB and DF regimes, which is followed by a rapid increase in the DF and FF regimes and a mild increase in the AP, IP and IC regimes. A jump in  $\bar{C}_d$  at  $L/D=4.6$  divides the IP and IC regimes, corresponding to the commencement of the fully developed in-phase co-shedding pattern. Compared with the downstream cylinders, the upstream cylinder has a smaller  $\bar{C}_d$ . The first decreasing then increasing trend is closely related to the variation of the upstream shear layers. While the decrease in  $\bar{C}_d$  in the SB regime is connected to the growth of base-bleed flow between the gap of the upstream and a downstream cylinder, the increase in  $\bar{C}_d$  from DF ( $L/D=1.4$ ) to IP ( $L/D=4.6$ ) is linked to the growth of the shear layers as well as vortices in the gap between the downstream cylinders. For  $L/D=1.0$ , the upstream-cylinder shear layers encircle the downstream cylinders, no flux going through the gap results in a low-pressure region between the cylinders, leading to a large  $\bar{C}_d$ .

The r.m.s. drag coefficient  $C'_d$  shown in figure 9(b) shows that the upstream cylinder  $C'_d$  is small regardless of the flow regime despite the fact that the borders between the regimes are characterized by a sudden drop or rise in  $C'_d$ . The value of  $C'_d$  of the upstream cylinder is zero in the DF and IP regimes. The value of  $C'_d$  is virtually equal for the two downstream cylinders. The value of  $C'_d$  of a downstream cylinder reaches a maximum value of 0.23 at  $L/D \approx 1.2$  where the free-stream-side vortices form closer to the base of the cylinders. The value of  $C'_d$  plummets at  $L/D=1.4$  and becomes small in the DF regime, which is attributed to the base-bleed flows postponing the roll-up of the free-stream-side shear layers. With a further increase in  $L/D$ , the value of  $C'_d$  increases in the FF regime due to the gap flow swing while levelling out in the AP, IP and AP regimes. Similar to  $\bar{C}_d$ ,  $C'_d$  jumps at  $L/D=4.6$ , caused by the transition from IP to IC flows. The value of  $C'_d$  of a downstream cylinder is consistently larger than that of the upstream cylinder except in the AP regime.

### 3.2.2. Lift coefficient

Figure 9(c) shows the variation in  $\bar{C}_l$  with  $L/D$ . The value of  $\bar{C}_l$  of the upstream cylinder is roughly zero for all  $L/D$ , no matter whether the wake is symmetric or not, with a trivial non-zero  $\bar{C}_l$  occurring in the DF regime. For the downstream cylinders, the value of  $\bar{C}_l$ , however, shows a significant dependency on  $L/D$ , becoming repulsive in the SB, DF and IC regimes while it is attractive in the regimes from DF to IP. The upstream shear layers enveloping the three cylinders cause low pressure on the free-stream-side of the downstream cylinders and lead to a repulsive  $\bar{C}_l$  in the SB and DF regimes. The  $\bar{C}_l$  magnitude attains a maximum of 0.55 at  $L/D=1.1$ . The occurrence of the attractive  $\bar{C}_l$  results from the upstream-cylinder shear layers entering into the gap. The free-stream-side shear layers are thus diminished due to the cutoff of the vorticity/momentum supplement from the upstream-cylinder shear layers (figure 4a-c). Another factor is that the front stagnation point of a downstream cylinder is located on the free-stream-side front surface (not shown here). In the IC regime, repulsive  $\bar{C}_l$  appears again, attributed to the upstream cylinder shielding that restricts the growth of the shear layers from the gap sides of the downstream cylinders. To summarize, the value of  $\bar{C}_l$  of a downstream cylinder is controlled by two counteracting factors: the added momentum effects and the shielding effects. In addition, the value of  $\bar{C}_l$  of the two downstream cylinders are the same in magnitude but opposite in sign except in the DF regime.

The value of  $C'_l$  of the upstream cylinder decreases with increasing  $L/D$  in the SB regime, being nearly zero in the regimes from DF to AP and small in the IP regime (figure 9d). While the nearly zero value is ascribed to the almost symmetric shear layers from the upstream cylinder, the small value results from the swing of the symmetric shear layers. A large  $C'_l$  prevails in the IC regime because of the formation of alternating vortices from the upstream-cylinder shear layers. Similar to its upstream cylinder counterpart, the value of  $C'_l$  of a downstream cylinder decreasing with increasing  $L/D$  in the SB regime becomes nearly zero in the DF regime. A rapid increase is identified in the FF and AP regimes ( $L/D = 2.0$ – $2.8$ ), followed by a drop at  $L/D = 2.8$  and a jump at  $L/D = 3.4$ . In the IC regime ( $L/D = 4.6$ – $6.0$ ), the value of  $C'_l$  is large and decreases with increasing  $L/D$ .

The values of  $\bar{C}_d$  and  $C'_l$  are different for the two downstream cylinders for  $5.0 \leq L/D \leq 5.2$ , which is attributed to the asymmetric wakes (figure 8b). It can be seen that Cylinder 2 is associated with the wider wake, leading to a larger  $C'_l$  and a smaller  $\bar{C}_d$  due to the vortex shedding occurring closer to the cylinder's upper and lower sides. On the contrary, Cylinder 3 is connected with the narrower wake, and thus has a smaller  $C'_l$  and a larger  $\bar{C}_d$ . Further evidence can be observed that the negative pressure around the two downstream cylinders is not the same, suggesting different vortex dynamics (not shown here).

In figure 9, the numerical results of Bao *et al.* (2010) are also presented for comparison purposes. The two sets of results agree very well, and the present results show much more detail due to the smaller increment in  $L/D$ .

### 3.2.3. Strouhal number

Figure 10 displays the variation of Strouhal number ( $St$ ) with  $L/D$ . The value of  $St$  is obtained from the power spectra of the fluctuating lift coefficients. Note that the Strouhal numbers of the downstream cylinders were equal for all  $L/D$  examined; for conciseness, only one of them is presented. The value of  $St$  is identical for the three cylinders in the SB, DF and FF regimes. It becomes minimum,  $St = 0.085$ , at  $L/D = 1.8$ . The value of  $St$  at the largest spacing ratio of  $L/D = 6.0$  is  $St = 0.152$ , which is 6.7% smaller than that for an isolated cylinder ( $St = 0.163$ ). The value of  $St$  is the largest in the second AP regime. A possible reason is that the near wake in the anti-phase pattern is narrower.

The Strouhal numbers of the three cylinders are the same in most of the cases, except for AP pattern (figure 10). In the AP pattern, the lift of the downstream cylinders shows single-frequency characteristics while the lift of the upstream cylinder features multiple frequencies. The dominant lift frequencies of the upstream and downstream cylinders verify the relationships of  $St_d - St_{u1} = St_{u2}$  and  $St_d + St_{u1} = St_{u3}$ , in which  $St_d$  is the dominant frequency of the downstream lift while  $St_{u1}$ ,  $St_{u2}$  and  $St_{u3}$  are the first three dominant frequencies of the upstream lift.

### 3.2.4. Phase lag between vortex sheddings from the two downstream cylinders

Figure 11(a) shows the phase lag  $\phi_{23}$  between the vortex sheddings from the two downstream cylinders, obtained from the cross-correlation between the fluctuating lift of the two downstream cylinders. In the SB flow,  $\phi_{23}$  is  $0^\circ$ , in-phase, resulting from the alternating vortex shedding occurring from the free-stream sides only. The gap flow deflection occurring in DF leads to a change in  $\phi_{23}$  from  $0^\circ$  (SB) to approximately  $180^\circ$  and increases further to approximately  $270^\circ$ . In the FF flow ( $L/D = 2.0$ – $2.5$ ), due to the instantaneous lift frequencies of the two downstream cylinders being unequal, the phase lag was not calculated. The AP

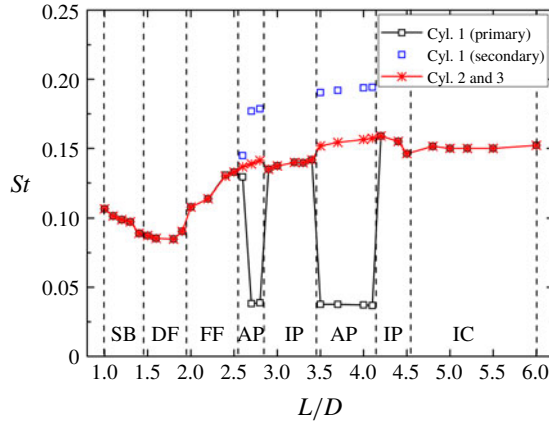


FIGURE 10. The Strouhal numbers of three cylinders versus the spacing ratio. The wake patterns are separated by the dashed line.

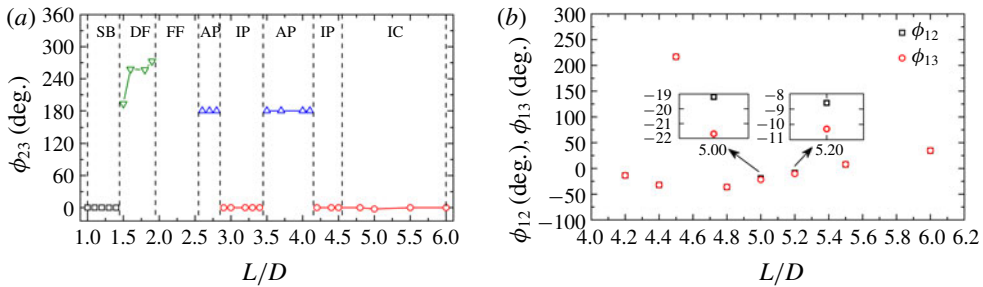


FIGURE 11. (a) The phase ( $\phi_{23}$ ) between two downstream cylinders. (b) The phases ( $\phi_{12}$  and  $\phi_{13}$ ) between Cylinders 1 and 2, and between Cylinders 1 and 3, respectively.

flow at  $L/D = 2.6-2.8$  and  $L/D = 3.5-4.1$  has  $\phi_{23} = 180^\circ$  while the IP flow at  $L/D = 2.9-3.4$  and  $L/D = 4.2-4.5$  corresponds to  $\phi_{23} = 0^\circ$  that also characterizes the IC flow at  $L/D = 4.6-6.0$ .

As mentioned above, the r.m.s. lift coefficients of the downstream cylinders show a significant drop at  $L/D = 4.5$  (see figure 9d). To elucidate the underlying mechanisms, the phase lags between Cylinders 1 and 2 ( $\phi_{12}$ ) and Cylinders 1 and 3 ( $\phi_{13}$ ) are presented in figure 11(b). It can be seen that, although  $\phi_{23}$  is roughly zero in the IP flow ( $L/D = 4.2-4.5$ , see figure 11a),  $\phi_{12}$  and  $\phi_{13}$  show much larger variations, close to in-phase at  $L/D = 4.2-4.4$  and anti-phase at  $L/D = 4.5$ . Because the anti-phase vortex-shedding pattern has a stronger interaction between the upstream and downstream cylinders, the shear layers of the upstream cylinder push the gap-side vortices shed from the downstream cylinders closer to their bases (see figure 7b) at  $L/D = 4.5$  than at  $L/D = 4.2-4.4$ , resulting in the much lower r.m.s. lift at  $L/D = 4.5$ . Moreover, in the IC flow,  $\phi_{12}$  and  $\phi_{13}$  are generally in in-phase and equal to each other except for small differences examined at  $L/D = 5.0$  and  $5.2$ .

### 3.2.5. The mean velocity and shearing rate of the gap flow

It is worth seeing how the flow through the gap varies with  $L/D$ . Figure 12(a) shows the time- and space-averaged streamwise velocity  $U_G/U (= (1/U) \int_{-0.5}^{0.5} \bar{u}d(y/G)$ ,

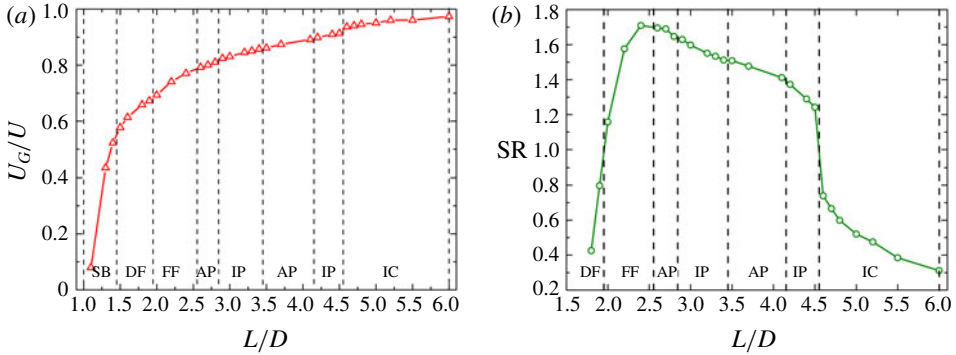


FIGURE 12. (a) The normalized time- and space-averaged streamwise velocity ( $U_G/U$ ) of the gap flow. (b) The normalized maximum shearing rate ( $SR = (D/U)(du/dy)$ ) of the gap flow profile between two side peaks. The flow patterns are separated by the dashed line.

where  $\bar{u}$  is the time-mean streamwise velocity) of the gap flow. The  $U_G/U$  grows with  $L/D$ ; the growth rate being very large in SB flow decreases in the successive flow regimes.

The stability of the upstream shear layers may dictate the flow around the two downstream cylinders and in the gap. Once the upstream-cylinder shear layers enter the gap, the streamwise velocity profile shows two peaks in the vicinity of the inner sides of the downstream cylinders and one trough at the middle of the gap (e.g. figure 4f). Figure 12(b) shows the maximum shearing rate  $SR (= (D/U)(du/dy))$  of the gap flow profile between the two side peaks. When  $L/D < 1.8$ , the gap flow profile is parabolic, without a centre trough. With increasing  $L/D$ , the shearing rate soars in the FF regime, indicating a rapidly boosted shearing instability. Therefore, the time scale for flip-flops reduces. The peak shearing rate ( $SR = 1.7$ ) is obtained at  $L/D = 2.4$ , corresponding to the smallest switching time scale indicated in figure 5. With a further increase in  $L/D$ , the shearing rate declines, with a rapid drop at the boundary between IP and IC flows. Generally, the shearing rate shows a first increasing then decreasing scenario with increasing  $L/D$ , which reflects a weak–strong–weak interaction between the upstream-cylinder shear layers and the downstream-cylinder gap-side shear layers. A strong interaction exists in the FF regime.

#### 4. The effects of the Reynolds number

The value of  $Re$  is always a key factor in the dynamics of flow past multiple cylinders. In this section, the  $Re$  effect on the hydrodynamic forces and flow structures is presented. For a clear presentation, results for six  $L/D = 1.2, 1.6, 2.5, 4.0, 4.5$  and  $5.0$  are presented, covering the six flow regimes discussed in § 3. For each  $L/D$ , the effect of  $Re$  is investigated in the range of  $Re = 50$ – $175$  with an interval of 25. For the flow past a stationary cylinder,  $Re = 50$  is close to the threshold of periodic vortex shedding, the Hopf bifurcation (Berger & Wille 1972; Huerre & Monkewitz 1990; Kumar & Mittal 2006; Étienne & Pelletier 2012), and  $Re = 175$  is slightly lower than the threshold of a three-dimensional wake (Miller & Williamson 1994; Barkley & Henderson 1996; Williamson 1996a).

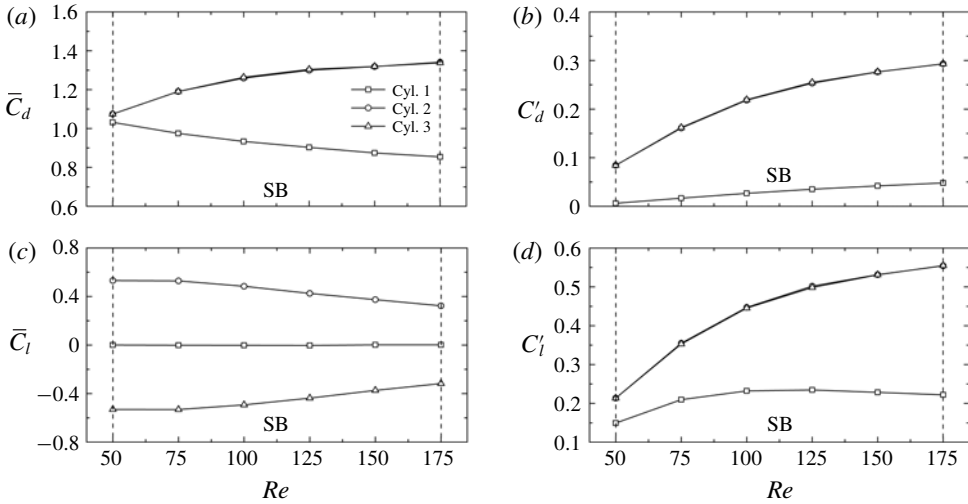


FIGURE 13. Fluid forces acting on three cylinders at  $L/D = 1.2$ .

4.1. Case  $L/D = 1.2$  – single bluff-body flow

Figure 13 shows the dependence on  $Re$  of the fluid forces of three cylinders at  $L/D = 1.2$ . The time-mean drag coefficients of the downstream cylinders, being identical to each other, increase with  $Re$  while that of the upstream cylinder decreases monotonically. As can be seen in figure 14, with increasing  $Re$ , stronger shear layers from the gap appear near the bases of the downstream cylinders, therefore the pressure becomes lower in gap side and base regions. As such, the value of  $\bar{C}_d$  and  $\bar{C}_l$  of the downstream cylinders increase and decrease, respectively, with  $Re$ . For the upstream cylinder, the decrease of  $\bar{C}_d$  is related to the waning viscous shear effects, following the  $Re$  effect on the value of  $\bar{C}_d$  of a single cylinder (Zdravkovich 1997). The value of  $C'_d$  increases with  $Re$  for all three cylinders, being smaller for the upstream cylinder than for a downstream cylinder (figure 13). This is related to the fact that an increase in  $Re$  leads to a greater flow through the gap and a stronger vortex shedding that shifts close to the base of the downstream cylinders. For the same reason, the value of  $C'_l$  of a downstream cylinder grows with  $Re$ , having a similar trend of  $C'_d$ . The value of  $C'_l$  of the upstream cylinder firstly increases with  $Re = 125$  and then declines very slowly. As in figure 14, the gap shear layers are hardly observed for  $Re \leq 75$ , getting thicker and stronger at  $Re \geq 100$ . At  $L/D = 1.2$ , the wake exhibits SB flow for the entire range of  $Re = 50-175$  examined. Figure 14 also shows the lift spectra of the three cylinders. With the increase in  $Re$ , the vortex-shedding frequency monotonically grows. For the downstream cylinders, a harmonic frequency, twice the fundamental one, appears, caused by the interaction of the gap flow with the vortex shedding. With increasing  $Re$ , the peak at the harmonic frequency increases, consistent with the fact that the interaction is intensified.

4.2. Case  $L/D = 1.6$  – single bluff-body, deflected and flip-flopping flows

Figure 15 shows the variations in fluid forces acting on the three cylinders at  $L/D = 1.6$ . The value of  $\bar{C}_d$  of each cylinder generally decreases for  $Re < 125$  and increases for  $Re > 125$ , with the exception that Cylinder 2 shows a local extremum at  $Re =$

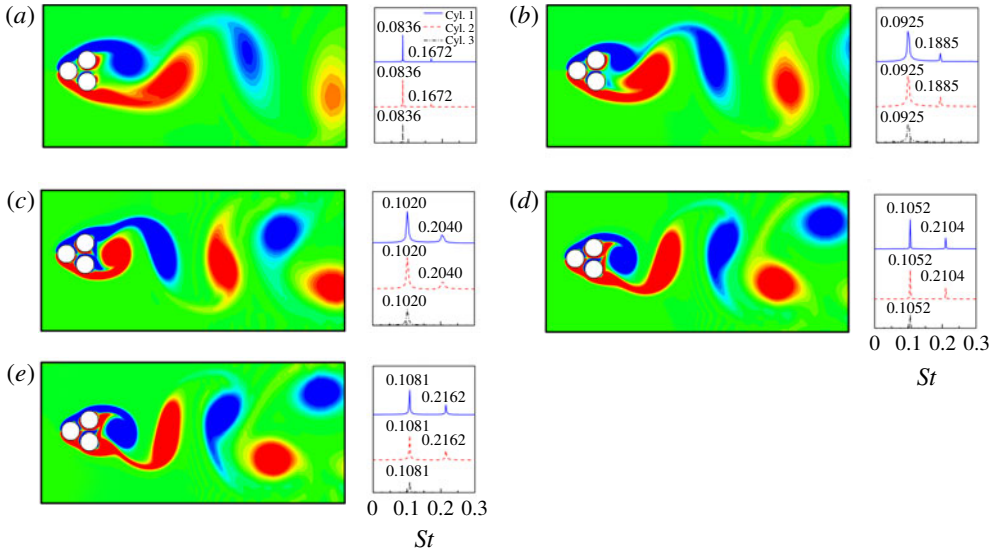


FIGURE 14. Vorticity fields (left) and spectra of the lift coefficients (right) at  $L/D = 1.2$ . (a–e) Represent the results at  $Re = 50, 75, 125, 150$  and  $175$ , respectively.

100 due to the deflected gap flow. The values of  $C_d$  and  $C_l$  generally increase with  $Re$  for all three cylinders, the downstream cylinders show a faster growth than the upstream cylinder at  $Re \geq 125$ . This can be attributed to the fact that, when  $Re \geq 125$  (FF flow), the swinging inner shear layers get rapidly stronger and closer to the base of the downstream cylinders with the increase of  $Re$ . The magnitudes of  $\bar{C}_l$  of the downstream cylinders decrease for  $Re < 150$  where lift forces are attractive. The lift forces, on changing their signs, become repulsive at  $Re > 150$ . Compared with the onset of the attractive lift at  $L/D = 1.9$  for  $Re = 100$ , the beginning of the lift attraction corresponds to a lower  $L/D = 1.6$  for  $Re = 150$ . On increasing  $Re$  from 50 to 175 the flow thus changes from SB to DF and DF to FF. As seen from the vorticity structures, the flow through the gap is enhanced with increasing  $Re$ , the gap shear layers elongate (figure 16a–c) and shed vortices (figure 16d–e). The flow structure change with  $Re$  (figure 16) bears similar characteristics to that with  $L/D$  (figures 2–4). Figure 16 also shows power spectra of the lift coefficients of the three cylinders at  $L/D = 1.6$  with varying  $Re$ . In the SB flow ( $Re = 50–75$ ),  $St$  increases with  $Re$ . The peak height ( $= 0.0149$ ) for Cylinder 2 is the same as that ( $= 0.0149$ ) for Cylinder 3, suggesting SB flow. In the DF flow ( $Re = 100$ ), the peak heights for Cylinders 2 and 3 are different, confirming that the gap flow is stably deflected, but vortex-shedding frequencies from the free-stream sides of the downstream cylinders are the same. In the FF flow regime ( $Re = 125–175$ ), multiple peaks are observed, indicating the unsteady interaction between the cylinders. A low frequency, related to the switching of the gap flow direction, is observed in the spectra of the two downstream cylinders in the flip-flopping regime.

#### 4.3. Case $L/D = 2.5$ – steady symmetric, steady asymmetric, flip-flopping and hybrid flows

Variations in fluid forces with  $Re$  are shown in figure 17 for  $L/D = 2.5$ . The value of  $\bar{C}_d$  of the upstream cylinder shows a decrease with  $Re$  except at  $Re = 100$ . The

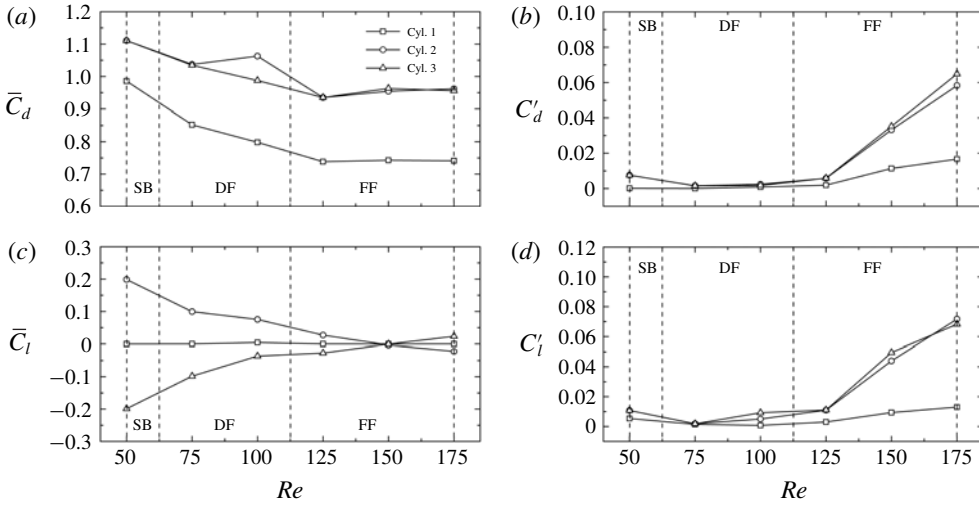


FIGURE 15. Fluid forces acting on three cylinders at  $L/D = 1.6$ .

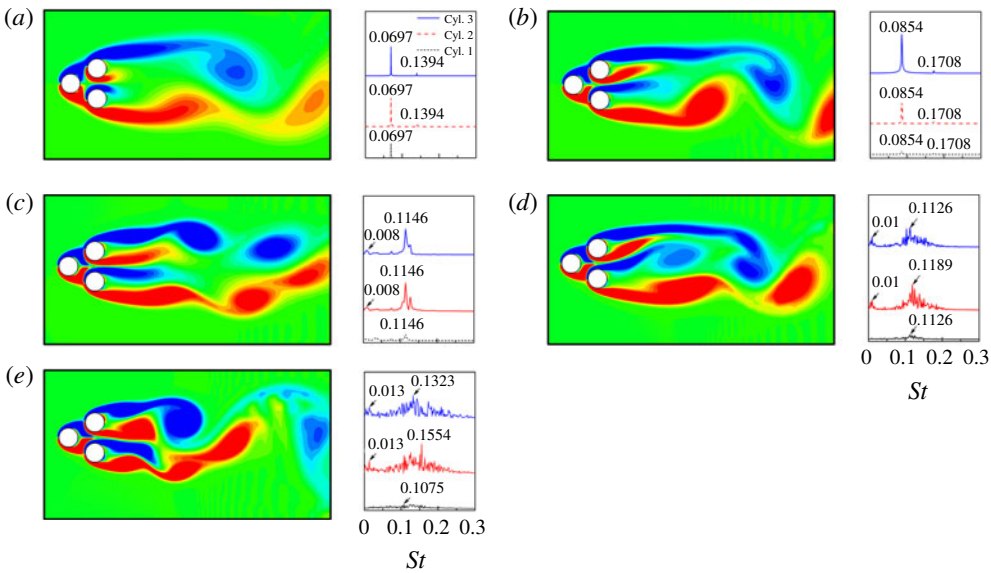
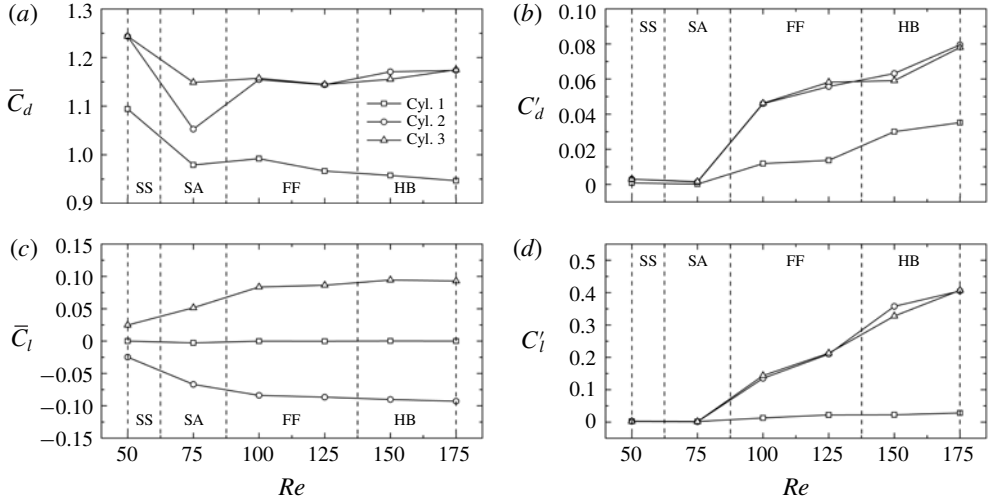


FIGURE 16. Vorticity fields (left) and spectra of the lift coefficients (right) at  $L/D = 1.6$ . (a–e) Represent the results at  $Re = 50, 100, 125, 150$  and  $175$ , respectively.

values of  $\bar{C}_d$  of the two downstream cylinders are substantially different at  $Re = 75$  while they are the same at  $Re = 50$  and  $100$ . The flows at  $Re = 50$  and  $75$  are steady, no vortex shedding occurring from the cylinders (figure 18a,b), but there is a very weak swinging of the shear layers. Correspondingly, the power spectra of lift show a very small peak at  $St = 0.0324$  for  $Re = 50$  and  $St = 0.0390$  for  $Re = 75$  (figure 18b). In fact, these low frequencies are non-physical, resulting from the limited downstream extension of the computational domain. The stability analyses of Rioni (2015) on the steady asymmetric flow past two side-by-side cylinders ( $Re = 68$  and

FIGURE 17. Fluid forces acting on three cylinders at  $L/D = 2.5$ .

$L/D = 1.7$ ) revealed that at least  $550D$  is needed for the downstream extension to properly converge the eigenvalues, due to a wavemaker structure slowly decaying in the far wake. In the present simulations, we found that when  $L_d \geq 200D$ , the small peaks are not observed, supporting the results of Rigoni (2015). The wake flow is symmetric at  $Re = 50$  and asymmetric at  $Re = 75$ ; they are therefore termed steady symmetric (SS) and steady asymmetric (SA). The flow is steady at  $Re = 50$  and  $75$  which can be further confirmed by  $C'_l \approx 0$  (figure 17d). It is symmetric and asymmetric at  $Re = 50$  and  $75$ , respectively, as further reflected in the same magnitudes ( $\bar{C}_l = \pm 0.025$ ) of  $\bar{C}_l$  for the two downstream cylinders at  $Re = 50$  and different magnitudes ( $\bar{C}_l = 0.052$  and  $-0.070$ ) at  $Re = 75$  (figure 17c). Both  $C'_l$  and  $C'_d$  swell when  $Re$  increases from  $75$  (figure 17b,d) as found for  $Re > 125$  at  $L/D = 1.6$  (figure 15b,d). The FF flow appears at  $Re = 100-125$ . The gap flow switching from one side to the other engenders two shedding frequencies for the downstream cylinders (figure 18). At  $Re = 150-175$ , the upstream cylinder sheds vortices at a lower frequency than the downstream cylinders, and the peaks are broad-banded for all cylinders. The near wake is alternately dominated by the FF and AP flows, and this regime is therefore termed the hybrid regime (HB).

To further explicate the HB flow, a wavelet transform of  $C_l$  time histories of the two downstream cylinders was carried out by using the complex Morlet wavelet – the most commonly used complex-valued wavelet. The non-dimensional frequency was set at 6 to avoid using the correction terms (Farge 1992). The same mother function was adopted in Zhao, Cheng & An (2012) to analyse the vortex-induced vibrations of an isolated circular cylinder in oscillatory flow. The discrete set of scales was chosen in a linear manner according to the frequency peak calculated using the fast Fourier transform. Figure 19(a) shows the time histories of  $C_d$  and  $C_l$  of the downstream cylinders at  $Re = 175$  and  $L/D = 2.5$  divided into region I (FF), region II (transition) and region III (AP). Figure 19(b,c) shows the contours of the real part of the wavelet transform of  $C_l$ , in which colour indicates the magnitude. The two frequencies are identical and nearly invariant with time in the AP flow, but show obvious fluctuations in the FF flow. Figure 19(d) shows the phase lag  $\phi_{23}$  between

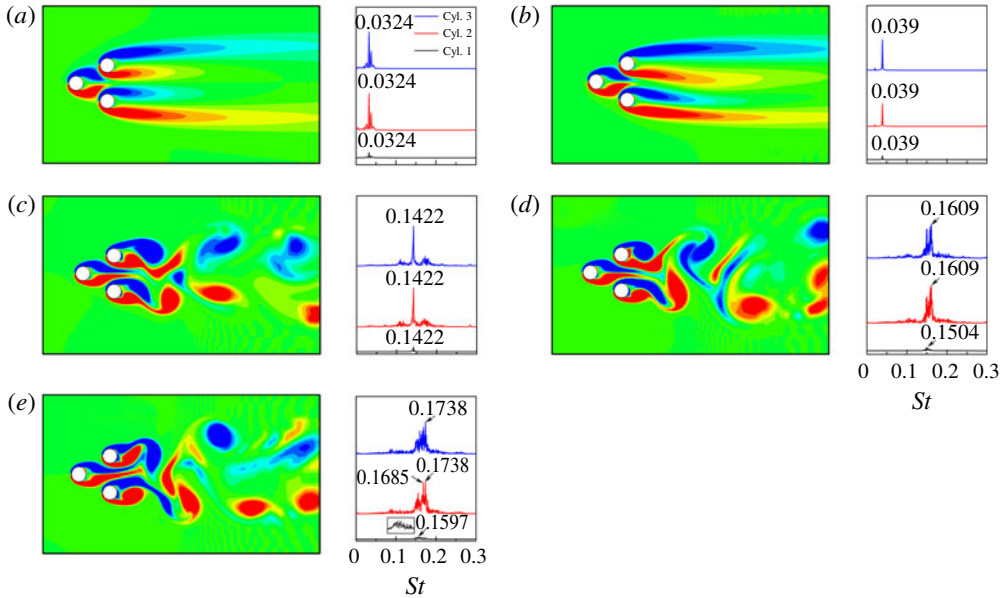


FIGURE 18. Vorticity fields (left) and spectra of the lift coefficients (right) at  $L/D = 2.5$ . (a–e) Represent the results at  $Re = 50, 75, 125, 150$  and  $175$ , respectively.

the  $C_l$  of two downstream cylinders. In the AP regime,  $\phi_{23}$  oscillates near  $180^\circ$  while in the FF regime  $\phi_{23}$  increases with large and irregular fluctuations owing to the fact the dominant frequencies are not the same.

#### 4.4. Case $L/D = 4.0$ – flip-flopping, anti-phase, in-phase and fully developed in-phase co-shedding flows

Figure 20 shows plots of the fluid forces acting on the three cylinders at  $L/D = 4.0$ . The value of  $\bar{C}_d$  of the upstream cylinder declines up to  $Re = 125$  followed by an increase with a further  $Re$  increase. At  $Re \leq 125$ , the upstream cylinder does not shed alternating vortices (figure 21a–c) and the decrease in  $\bar{C}_d$  with  $Re$  is caused by the declining viscous shear stress. However, at  $Re > 125$ , vortices formed in the gap and the vortex cores approach the base of the upstream cylinder with increasing  $Re$  (figure 21d,e) and, as a consequence,  $\bar{C}_d$  rises. The value of  $\bar{C}_d$  of the downstream cylinders generally decreases with  $Re$  except for a small increase at  $Re = 125$  related to the changing wake patterns. Similarly, values of  $C'_d$  and  $C'_l$  of the upstream cylinder are small for  $Re < 125$  and both increase for  $Re > 125$ . However, those for the downstream cylinders significantly increase. An attractive  $\bar{C}_l$  acts on the downstream cylinders in the range of  $Re \leq 125$  and turns into a repulsive one at  $Re \geq 150$ . Figure 21 shows the dependence of the wake flow on  $Re$  at  $L/D = 4.0$ . At  $Re = 50$ , the FF flow with a long switching period of approximately 40 vortex-shedding periods is observed. Different from the FF flow at a smaller  $L/D$ , the wake does not show a biased gap flow but has different vortex formation lengths, owing to the weak interference between the downstream cylinders at a larger  $L/D$ . At larger  $Re$ , the wake shows the AP flow at  $Re = 75$ – $100$ , the IP flow at  $Re = 125$  and the IC flow at  $Re = 150$ – $175$ .

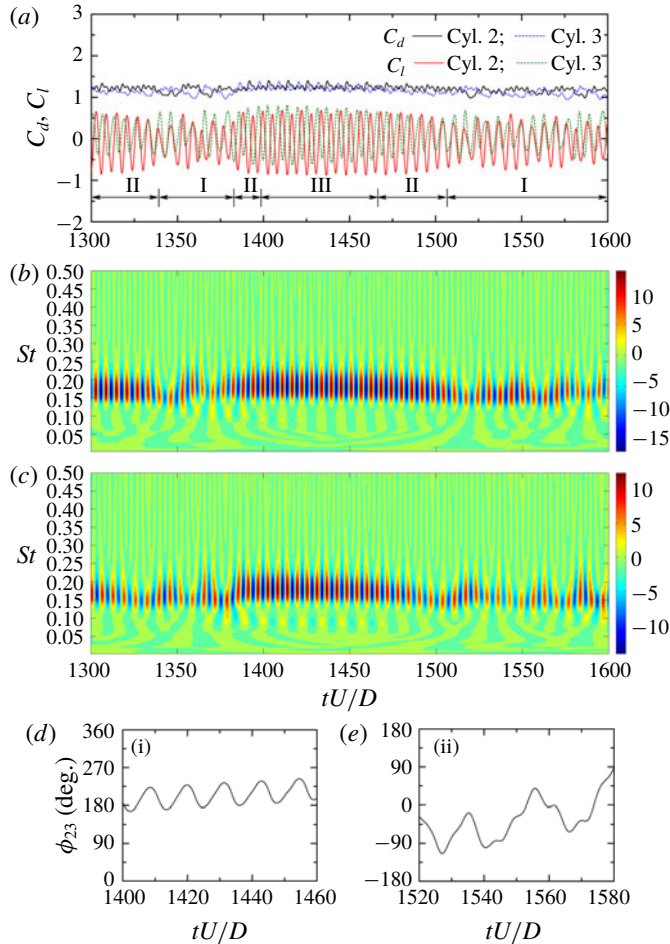


FIGURE 19. Flow past three cylinders at  $Re = 175$  and  $L/D = 2.5$ . (a) Time histories of the drag and lift coefficients of two downstream cylinders, (b) the real part of the wavelet transform of the lift coefficient of Cylinder 2, (c) the real part of the wavelet transform of the lift coefficient of Cylinder 3 and (d) the phase difference between the two downstream cylinders. Regions I, II, III denote regimes of the flip-flopping flow, transition and anti-phase flow, respectively.

#### 4.5. Case $L/D = 4.5$ – flip-flopping, anti-phase, in-phase and fully developed in-phase co-shedding flows

The fluid forces, lift spectra and wake patterns at  $L/D = 4.5$  are quite similar to those at  $L/D = 4.0$ . For the sake of conciseness, the results are not presented here. An obvious difference is that the attractive lift region ends at  $Re = 100$ , which is smaller than  $Re = 125$  for  $L/D = 4.0$ .

#### 4.6. Case $L/D = 5.0$ – anti-phase, in-phase and fully developed in-phase co-shedding flows

Shown in figure 22 are the fluid forces acting on the three cylinders at  $L/D = 5.0$  with varying  $Re$ . The value of  $\bar{C}_d$  of the upstream cylinder shows a significant drop

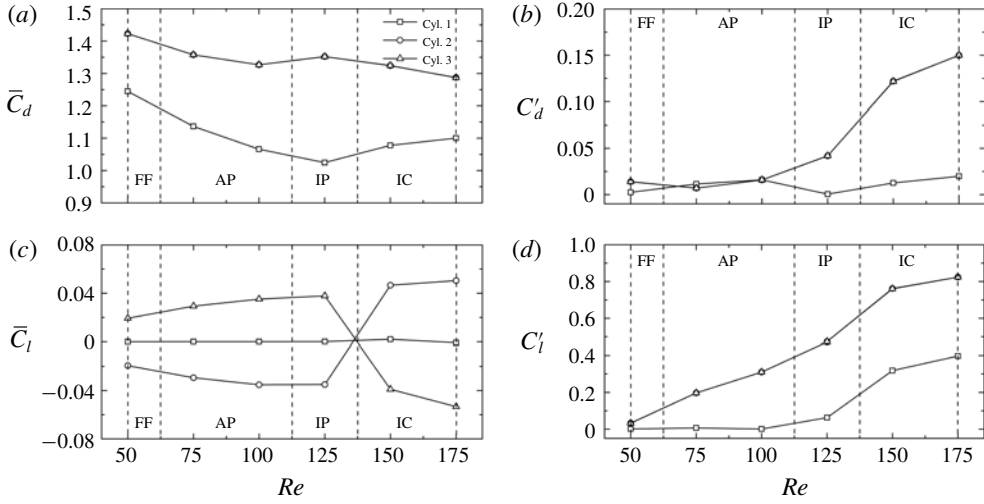


FIGURE 20. Fluid forces acting on three cylinders at  $L/D = 4.0$ .

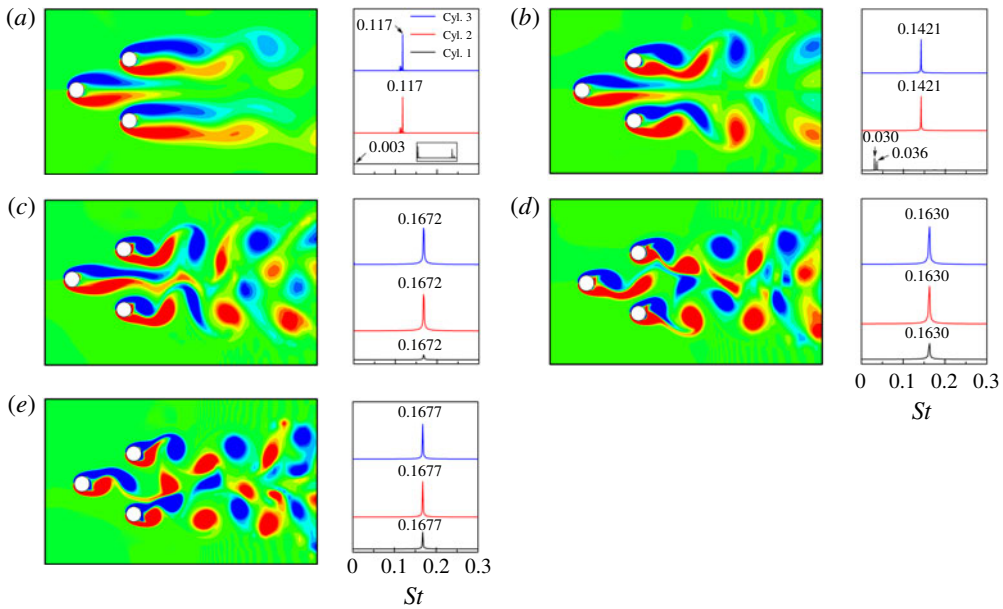


FIGURE 21. Vorticity fields (left) and spectra of the lift coefficients (right) at  $L/D = 4.0$ . (a–e) Represent the results at  $Re = 50, 75, 125, 150$  and  $175$ , respectively.

between  $Re = 50$  and  $75$ , levelling out for  $Re > 75$ . For the downstream cylinders,  $\bar{C}_d$  displays a generally decreasing trend except for a small increase between  $Re = 75$  and  $100$ . This is quite similar to the variation in  $\bar{C}_d$  at  $L/D = 4.0$ . It should be pointed out that the  $\bar{C}_d$  values of the two downstream cylinders are not identical at  $Re = 100$ – $175$ , because the wake downstream becomes asymmetric (figure 23c–e). The value of  $C'_d$  of a downstream cylinder increases with  $Re$  up to  $Re = 100$  and then levels out while  $C'_l$  further increases after  $Re = 100$ . The variations in  $\bar{C}_l$ ,  $C'_d$  and  $C'_l$  for all three cylinders

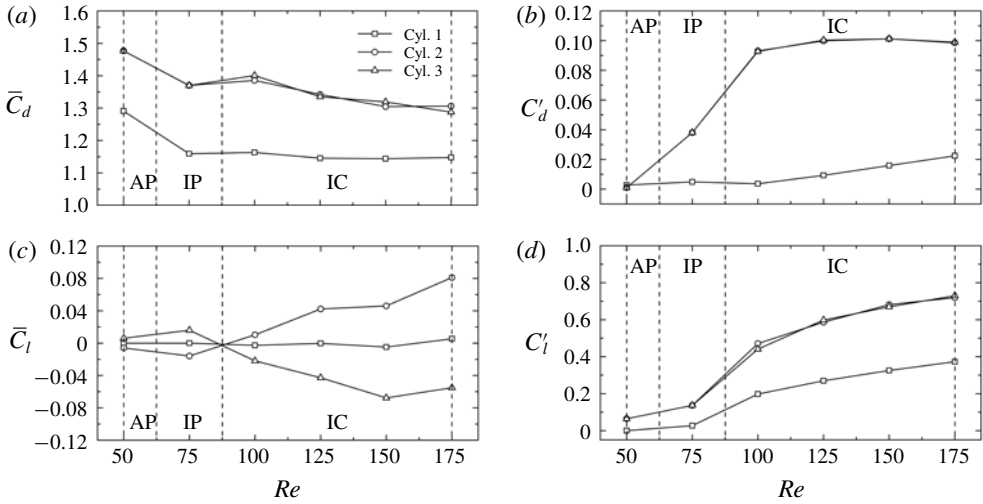


FIGURE 22. Fluid forces acting on three cylinders at  $L/D = 5.0$ .

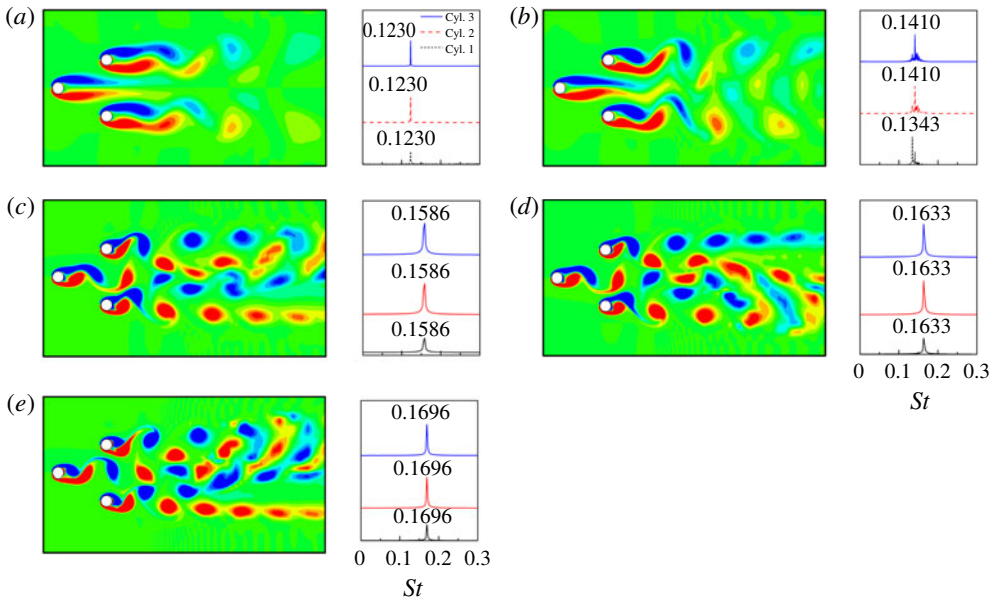


FIGURE 23. Vorticity fields (left) and spectra of the lift coefficients (right) at  $L/D = 5.0$ . (a–e) Represent the results at  $Re = 50, 75, 125, 150$  and  $175$ , respectively.

with  $Re$  are very similar to those with  $L/D$  in AP, IP and IC ( $L/D > 3.5$ ) in figure 9, explaining the flow modification from AP to IP and then to IC with increasing  $Re$  (figure 22). The observation suggests that the effect of increasing  $L/D$  on the flow is similar to that of increasing  $Re$ . Figure 23 displays the lift spectra of three cylinders at  $L/D = 5.0$ . At a given  $Re$ ,  $St$  is identical for the three cylinders, except at  $Re = 75$ . An increase in  $Re$  complements a growth in  $St$ .

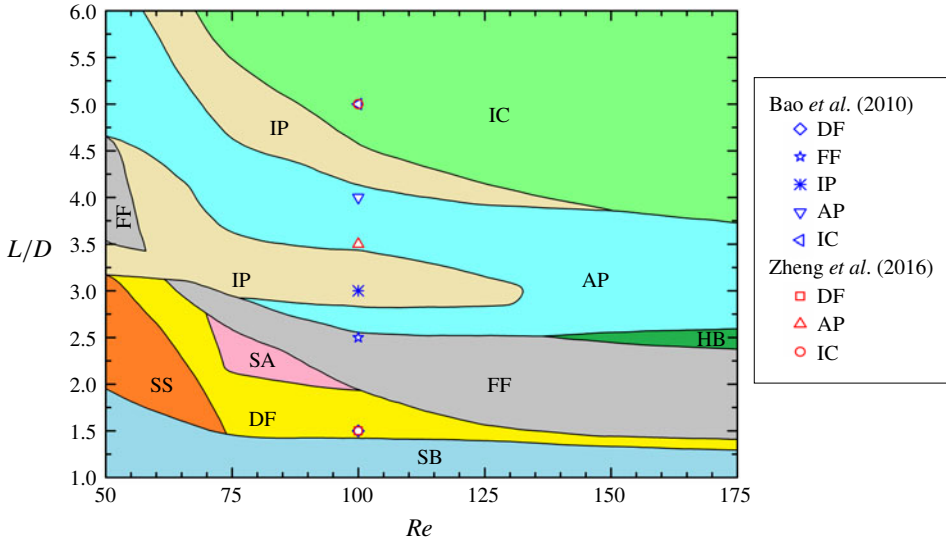


FIGURE 24. Flow regimes of flow past three circular cylinders in the parametric space of  $Re(=50-175)$  and  $L/D(=1.0-6.0)$ . The boundary between two adjacent flow patterns is approximately determined by using the midpoint of two adjacent data points. SS, steady symmetric flow; SA, steady asymmetric flow; HB, hybrid flow.

### 5. Dependence of flow on $Re$ and $L/D$ and connection to fluid forces

In order to provide a detailed view of the flow around the three cylinders and their connections to fluid forces, more cases within the parametric space of  $Re = 50-175$  and  $L/D = 1.0-6.0$  were carried out. Small increments in  $Re$  and  $L/D$  were adopted as  $\Delta Re = 5$  and  $\Delta L/D = 0.1$ . A map of the flow regime with distinct boundaries is given in figure 24. Nine flow patterns are observed: steady symmetric flow, steady asymmetric flow, single bluff-body flow, deflected flow, flip-flopping flow, in-phase flow, anti-phase flow, fully developed in-phase co-shedding flow and hybrid flow. It can be seen that SB and IC emerge in low and high- $L/D$  regions, respectively. The DF regime is observed in a low- $Re$  and low- $L/D$  region. The SA regime exists in a slightly larger  $L/D$  region compared with DF, while SS appears in a region left of DF and SA with a lower  $Re$ . FF dominates the space with a moderate  $L/D$  and a large  $Re$  or the space with a low  $Re$  and a large  $L/D$ . Increasing  $L/D$  transforms FF to IP when  $Re$  is low, but to AP when  $Re$  is high. Between FF and AP, there exists a narrow strip region of HB. In this sense, HB can be taken as a transition between FF and AP. As discussed in § 3, AP exists in two separated ranges when  $Re = 100$ . However, these two regions for AP are connected and merge into one when  $Re$  is high. Between AP and IC, the second IP region is evident. The flow regimes reported in Bao et al. (2010) and Zheng et al. (2016) are superimposed in figure 24 for comparison purposes. The flow regime identification agrees very well with those in Bao et al. (2010) and Zheng et al. (2016).

Shown in figure 25 are the contours of the fluid forces acting on the three cylinders, superimposed by the flow partition map. The value of  $\bar{C}_d$  of the upstream cylinder is large in the SB and IC regimes while it is small in the mid- $L/D$  region dominated by the other flow regimes. The largest  $\bar{C}_d$  is achieved at the top-left corner with low  $Re$  and high  $L/D$ . This is attributed to the significant viscous effects in low- $Re$  flows

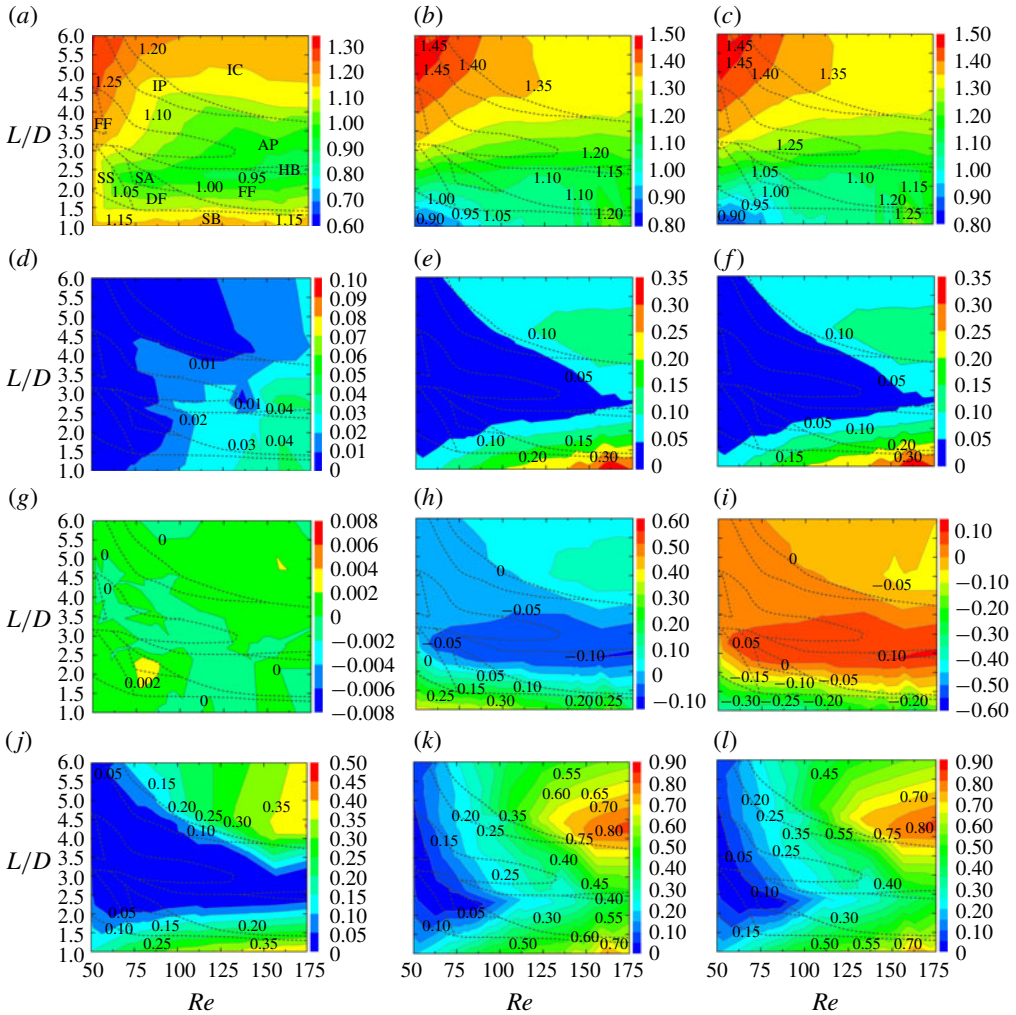


FIGURE 25. Fluid forces acting on three cylinders versus  $Re (= 50-175)$  and  $L/D (= 1.0-6.0)$ . The rows, from left to right, represent the results of Cylinders 1, 2 and 3, respectively. (a-c) Mean drag, (d-f) r.m.s. drag, (g-i) mean lift and (j-l) r.m.s. lift.

and the weak interference between the cylinders. In the entire domain, the value of  $\bar{C}_d$  is more sensitive to  $L/D$  than to  $Re$ . The  $Re$  effect on  $\bar{C}_d$  largely appears for  $Re < 125$ , as such, the flow patterns are densely distributed in this range of  $Re$ . Similar to its upstream-cylinder counterpart, the value of  $\bar{C}_d$  of the downstream cylinders is less dependent on  $Re$  than on  $L/D$  (figure 25b,c). For  $L/D > 3.5$ ,  $\bar{C}_d$  declines with increasing  $Re$ , while an opposite scenario is observed for  $L/D < 3.5$  where the  $\bar{C}_d$  grows with  $Re$ . Now  $\bar{C}_d$  is minimum at  $L/D = 1.0, Re = 50$ .

The  $C'_d$  distribution in the  $L/D - Re$  plane reflects that the value of  $C'_d$  of the upstream cylinder is less affected by  $L/D$  than by  $Re$ . The value of  $C'_d$  increases with  $Re$  and declines with  $L/D$ . For the downstream cylinders, the value of  $C'_d$  first decreases then increases with increasing  $L/D$ , showing low values at mid- $L/D$  where the flow interference is strong. The largest  $C'_d$  exists in the SB regime with high  $Re$ .

The value of  $\bar{C}_l$  of the upstream cylinder is trivial in the whole parametric plane with a small non-negligible region in the SA and DF regimes due to the deflected gap flow. The downstream cylinders undergo attractive  $\bar{C}_l$  (negative and positive  $\bar{C}_l$  for Cylinders 2 and 3, respectively) in an intermediate  $L/D$  range covering the regimes of IP, AP, FF and HB. The value of  $\bar{C}_l$  is repulsive at the bottom (SB, DF, SS regimes) and on the top-right corner (IC regime) of the parametric plane. The upper boundary between attractive and repulsive  $\bar{C}_l$  closely follows the boundary dividing the AP/IP and IC regimes while the lower boundary crosses the SS, DF and FF regimes. Again, the contour lines are generally horizontal, indicating that the  $Re$  effect is less prominent than  $L/D$ .

Upon comparing figure 25(*h,j*), it is found that the value of  $C'_l$  of the upstream cylinder is small in the attractive  $\bar{C}_l$  region. This is because, when the shear layers of the upstream cylinder go through the gap, this not only causes an attractive lift force on the downstream cylinders but also attenuates the fluctuating lift on the upstream cylinder due to the non-swinging shear layers. Large  $C'_l$  of the upstream cylinder is found in the IC and SB regimes. However, the values of  $C'_l$  show a strong dependency on  $L/D$  in the SB regime but on  $Re$  in the IC regime. For the downstream cylinder, the value of  $C'_l$  is a strong function of both  $Re$  and  $L/D$  in the IC regime, maximum  $C'_l$  occurring at  $Re = 175$ ,  $L/D = 4.3$ , while small  $C'_l$  corresponds to the DF, SA, SS and FF patterns.

## 6. The effects of the three-dimensionality

In this section, we aim at exploring how the three-dimensionality develops and its influences on the hydrodynamics and vortical structures behind the three cylinders. For the flow past a single circular cylinder, three-dimensional vortical structures appear when  $Re$  is larger than 193 (Williamson 1996*b*; Jiang *et al.* 2016*a*). Mode A dominates when  $Re$  is smaller than 230 and mode B emerges afterwards (Williamson 1996*a*; Jiang *et al.* 2016*a,b*). The coexistence of the two modes (A and B) is observed in the range of  $Re = 230$ – $250$ . In this  $Re$  range, the occurrence probability of mode B increases significantly with increasing  $Re$  (Jiang *et al.* 2016*a*). Subsequently, mode B becomes the only mode when  $Re$  exceeds 260. In this section,  $Re = 300$  is selected to understand the development of three-dimensional vortical structures and their influences on the flow dynamics. In the three-dimensional simulations, the mesh resolution in the  $x$ – $y$  plane is the same as that in the two-dimensional simulations. In the spanwise ( $z$ -direction) direction, the cylinder length is  $12D$  which is verified to be long enough for the adopted  $Re$  (Jiang *et al.* 2016*a,b*; Gao *et al.* 2019). A uniform mesh is applied in the  $z$ -direction with a resolution of  $\Delta z = 0.0625D$ . The validation of the 3-D simulation for a single cylinder at  $Re = 300$  is provided in the Appendix. The present results show good agreement with the numerical and experimental results in the literature. Based on the 2-D results in the previous sections, eight spacing ratios in the range of  $L/D = 1.2$ – $5.0$  are selected. The time histories, statistics and spectra of the drag and lift coefficients are presented along with the corresponding wake structures. Comparisons with the 2-D results are made wherever possible to demonstrate the influence of the three-dimensionality on the flow and underlying physics.

### 6.1. The $C_d$ and $C_l$ temporal histories and wake patterns

Figure 26 shows time histories of the lift and drag coefficients averaged over the cylinder span while figure 27 displays the corresponding vortex-shedding patterns

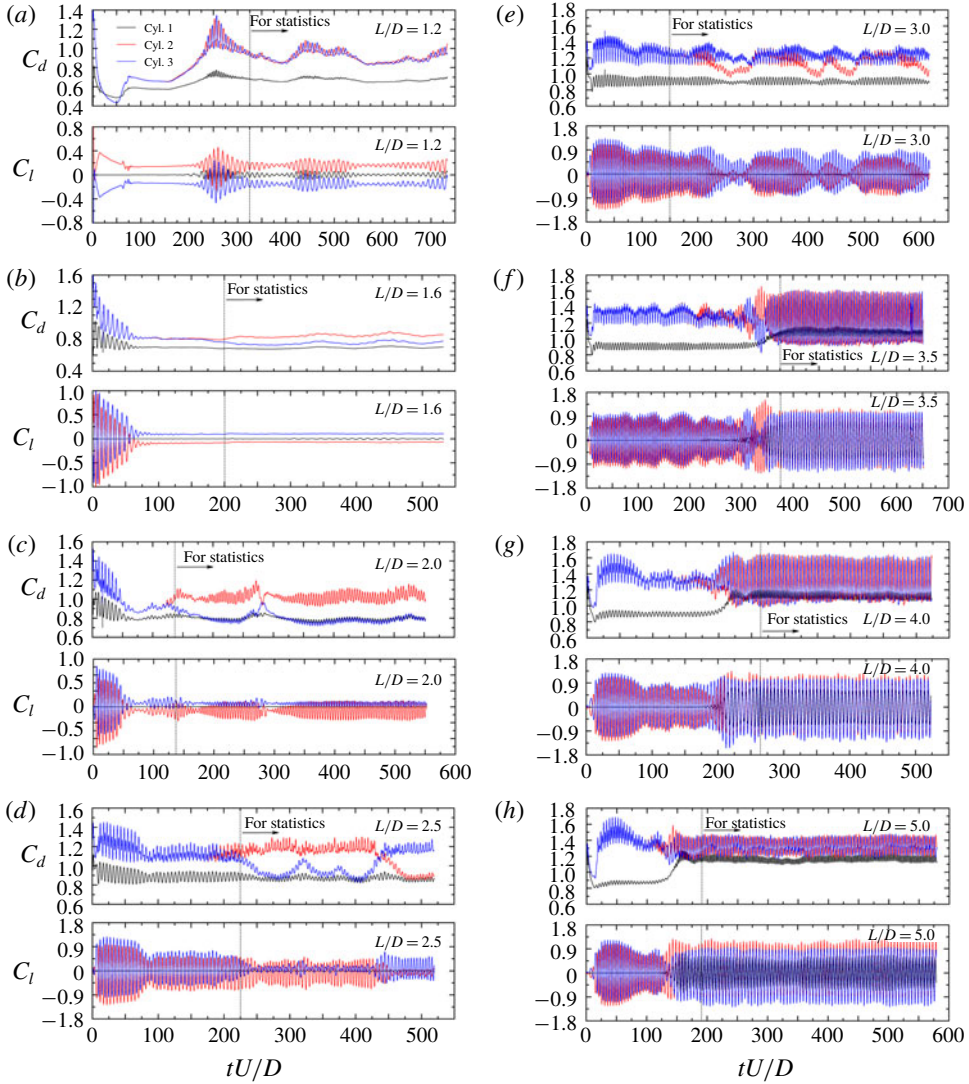


FIGURE 26. Time histories of the drag and lift coefficients of three cylinders at different  $L/D(= 1.2-5.0)$  and  $Re = 300$ .

when the flow is statistically stable. The  $C_d$ ,  $C_l$  and flow patterns are dependent on  $L/D$ .

The value  $L/D=1.2$  lies in SB regime. The force histories display some similarities with those from 2-D simulation at  $Re = 100$  (see figure 2g), including the in-phase  $C_l$  and anti-phase  $C_d$  of the two downstream cylinders, and smaller time-mean  $C_d$  for the upstream cylinder than the downstream cylinders. The vortex shedding occurs in mode B, with fully developed streamwise vortical filaments (Williamson 1996a), as shown in figure 27(a). To clearly show the spanwise vortices, the 3-D instantaneous flow field is averaged over the cylinder span, and the corresponding  $z$ -vorticity field is obtained, as shown in the second and fourth columns of figure 27. The upstream-cylinder-generated shear layers reattaching on the downstream cylinders roll up in the

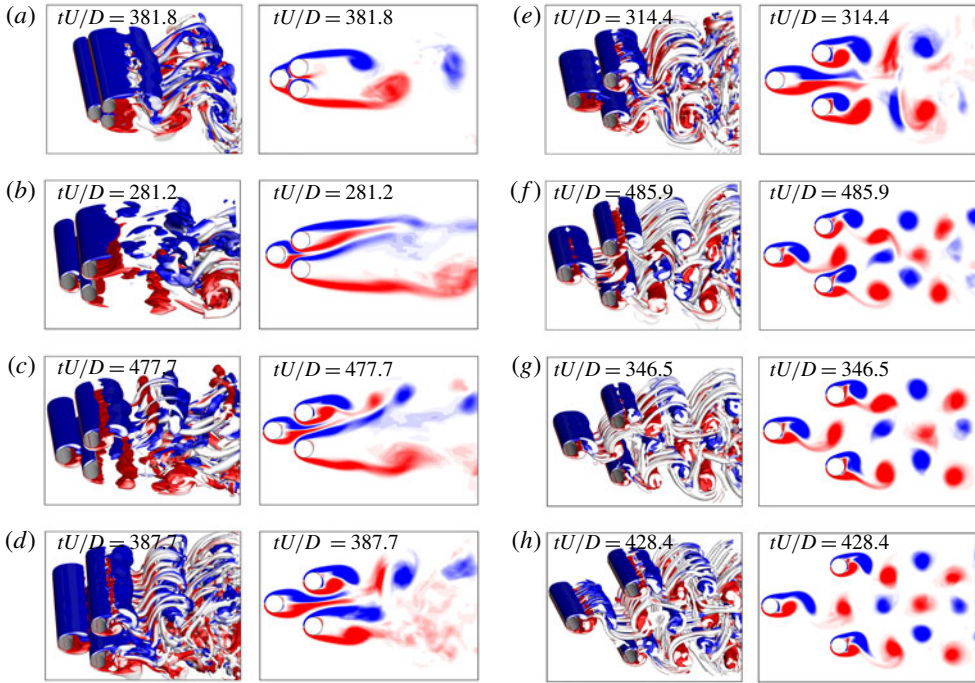


FIGURE 27. The vorticity contours of flow past three cylinders at  $Re = 300$  and (a)  $L/D = 1.2$ , (b)  $L/D = 1.6$ , (c)  $L/D = 2.0$ , (d)  $L/D = 2.5$ , (e)  $L/D = 3.0$ , (f)  $L/D = 3.5$ , (g)  $L/D = 4.0$  and (h)  $L/D = 5.0$ . Isosurfaces  $\lambda_2 = -0.2$ . The second and fourth columns represent the spanwise-averaged vorticity contours.

wake. The reattachment occurring on the upper front surface leaves a very weak flow through the gap. This is similar to what is observed at  $Re = 100$  in figure 2(c), except that the vortex formation length is substantially longer at  $Re = 300$ . Time-mean and fluctuating forces on the cylinders are thus smaller at  $Re = 300$  than at  $Re = 100$  (figures 2 and 26).

At  $L/D = 1.6$  (DF regime),  $C_d$  of Cylinder 2 is consistently smaller than that of Cylinder 3, which resembles DF at low  $Re$  (figure 3h). Compared with those at  $L/D = 1.2$ , the streamwise vortical filaments at  $L/D = 1.6$  are mainly observed farther downstream. Although breaking up in the 3-D plot, the shear layers are clearly discernible in the spanwise-averaged vorticity field, with the gap flow stably deflecting upward. The vortex formation length is, however, comparable between the 2-D and 3-D flows (figures 3a-c, 27b), while the gap flow intensity significantly increases in the 3-D flow.

The  $L/D = 2.0$  and 2.5 are categorized as FF regime because  $C_d$  and  $C_l$  switch irregularly and occasionally between two states – one of the fundamental features of the flip-flopping phenomenon. The flip-over period is, however, longer in the 3-D flow than in the 2-D flow (figures 4g, 26c,d). We also conducted 2-D simulations at  $L/D = 2.0$  and 2.5 with  $Re = 300$  and observed that the flip-over interval is only several vortex-shedding periods as found for  $Re = 100$ . This difference is linked to the presence of the mode B instability (Mittal & Balakandar 1995; Brede, Eckelmann & Rockwell 1996; Williamson 1996a). Zdravkovich (1997) stated that the vortices accompanied by the mode B instability appear close to the central plane and the

wake becomes narrower, which may lead to a weaker flow interference between two downstream cylinders. With increasing  $L/D$ , the flip-over period shortens, as found for the 2-D flow (figure 5). The deflection angle of the gap flow is obviously larger than the 2-D FF counterpart (figures 4*a-c*, 27*c*).

When  $L/D$  is increased to 3.0, the  $C_d$  and  $C_l$  histories display that AP and FF flows compete with each other, with the FF flow dominating the AP flow. Similar to the 2-D flow at  $L/D = 2.5$  and  $Re = 150-175$ , this flow is classified as HB flow. However, in the 2-D HB flow, the AP flow dominated the FF flow (figure 19). This can be attributed to the stronger flow instability caused by the higher  $Re$  and three-dimensional vortical structures in the 3-D flow. Figure 27(*d*) shows the vortical structures at a time instant corresponding to the AP flow. The flow is basically symmetric about the wake centreline in the near wake, becoming asymmetric after three vortex-shedding lengths.

The IC flow is identified at  $L/D \geq 3.5$ . The lift forces of the two downstream cylinders are in phase while the drag forces of the same cylinders are anti-phase with comparable oscillation amplitudes. With increasing  $L/D$ , the onset of the IC flow happens earlier (shorter time required to get the flow fully developed) because the enhanced vortices from the upstream cylinder coordinate the vortex shedding of the downstream cylinders. Three parallel vortex streets form in the wake of the 3-D flow (figure 27*f-h*). The 2-D simulation done at the same  $L/D$  and  $Re$  produced only two parallel vortex streets (not shown). The lateral deflection of vortices as found in the 2-D flow (figure 8) does not exist in the 3-D flow (figure 27*f-h*). In the 3-D wake, the two side vortex streets are clearly wider than the middle vortex street. Now the upstream cylinder clearly generates streamwise filaments before the downstream cylinders.

The features of 3-D wake flow can be summarized as follows. Five flow regimes are observed, i.e. SB ( $L/D = 1.2$ ), DF ( $L/D = 1.6$ ), FF ( $L/D = 2.0-2.5$ ), HB ( $L/D = 3.0$ ) and IC ( $L/D = 3.5-5.0$ ). The presence of the three-dimensional vortical structures leads to differences not only in the wake patterns themselves but also in the corresponding  $L/D$  ranges. For example, the HB regime occurs at  $L/D = 3.0$  for the 3-D flow while it exists at  $L/D = 2.5$  ( $Re = 175$ ) for the 2-D flow. However, all the wake patterns in the 3-D flow are observed in the 2-D flow, which suggests that the three-dimensionality of the flow may slightly alter the wake patterns and  $L/D$  ranges, but does not lead to a new one. In this context, the wake patterns observed in the 2-D flow can provide a good reference for high- $Re$  3-D flows.

## 6.2. Statistics and spectral features of $C_d$ and $C_l$

Figure 28 shows the time- and spanwise-averaged lift and drag coefficients of the cylinder at  $L/D = 1.2-5.0$ ,  $Re = 300$ . The flow regimes are separated by the vertical dashed lines. The  $\overline{C_d}$  of all three cylinders generally increases with  $L/D$  while the two downstream cylinders undergo repulsive lift for  $L/D < 1.75$ , attractive lift  $1.75 < L/D < 4.1$  and repulsive lift for  $L/D > 4.1$  (figure 28*a,c*). The  $C'_d$  of the downstream cylinders decreases between the SB and DF regimes and then grows in the FF regime, reaching a minimum in the DF regime. A drop in  $C'_d$  occurs at the boundary between FF and HB while a jump distinguishes the HB and IC regimes. The  $C'_d$  monotonically declines in the IC regime. The  $C'_d$  of the upstream cylinder is relatively small in the entire  $L/D$  range. The upstream cylinder  $C'_l$  is very small in the SB to HB regimes ( $L/D \leq 3.0$ ) and large in the IC regime; a jump in  $C'_l$  marks the boundary between the HB and IC regimes. It should be noted that the force coefficients in the FF and HB

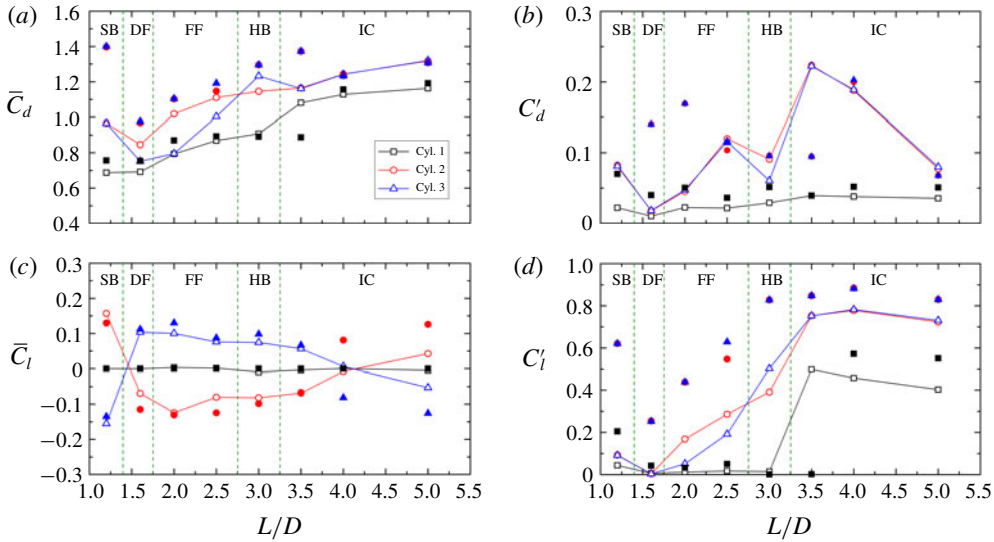


FIGURE 28. Fluid forces acting on three cylinders at  $L/D = 1.2–5.0$  and  $Re = 300$ . The open and solid symbols denote the results of 3-D and 2-D simulations. The wake patterns of 3-D results are divided through the vertical lines.

regimes are not identical for the two downstream cylinders, which can be attributed to the aperiodic flow and insufficiently long simulation time for averaging.

For comparison purposes, 2-D simulations at  $Re = 300$  were also carried out and the force coefficients are superimposed in figure 28. The two sets of results show similar trends, despite the fact that the 2-D simulations mostly overestimate the forces.

Shown in figure 29 are the power spectra of the lift coefficients at different  $L/D$ . In the SB regime ( $L/D = 1.2$ , figure 29a), the dominant lift frequencies of the three cylinders are identical at  $St = 0.104$ , and the second harmonic is observed for the downstream cylinders, similar to the 2-D results at  $Re = 100$ . At  $L/D = 1.6$  (DF flow), the dominant frequencies of the downstream cylinders and the upstream cylinder are different,  $St = 0.0094$  and  $0.0801$ , respectively (figure 29b). Indeed, the lift forces of the cylinders barely fluctuate in the DF regime. At  $L/D = 2.0$  (FF flow),  $St = 0.2368$  for each cylinder, and the corresponding peak is small for the upstream cylinder (figure 29c). However, a tiny spike at  $St = 0.0082$ , representing the flip-flopping frequency, can also be observed for the downstream cylinders. The non-dimensional flip-over period is calculated as  $0.2368/0.0082 \approx 30$ , indicating that the flip-over occurs every 30 vortex-shedding cycles. A similar observation is made at  $L/D = 2.5$  (figure 29d). In the HB flow ( $L/D = 3.0$ ), in addition to the identical  $St = 0.1872$  for the three cylinders, a tiny spike exists at  $St = 0.0051$  (figure 29e). Again, the latter  $St$  stems from the switch of the gap flow direction in the HB flow. When  $L/D \geq 4.0$ , all three cylinders have the same dominant frequency, with a small harmonic existing on the spectra of the downstream cylinders (figure 29g,h). The  $L/D = 3.5$  case is a transitional case where the dominant frequencies of the upstream and downstream cylinders are unequal.

## 7. Conclusions

The flow past three circular cylinders in equilateral-triangular arrangements was numerically investigated. The immersed boundary method was utilized to deal with

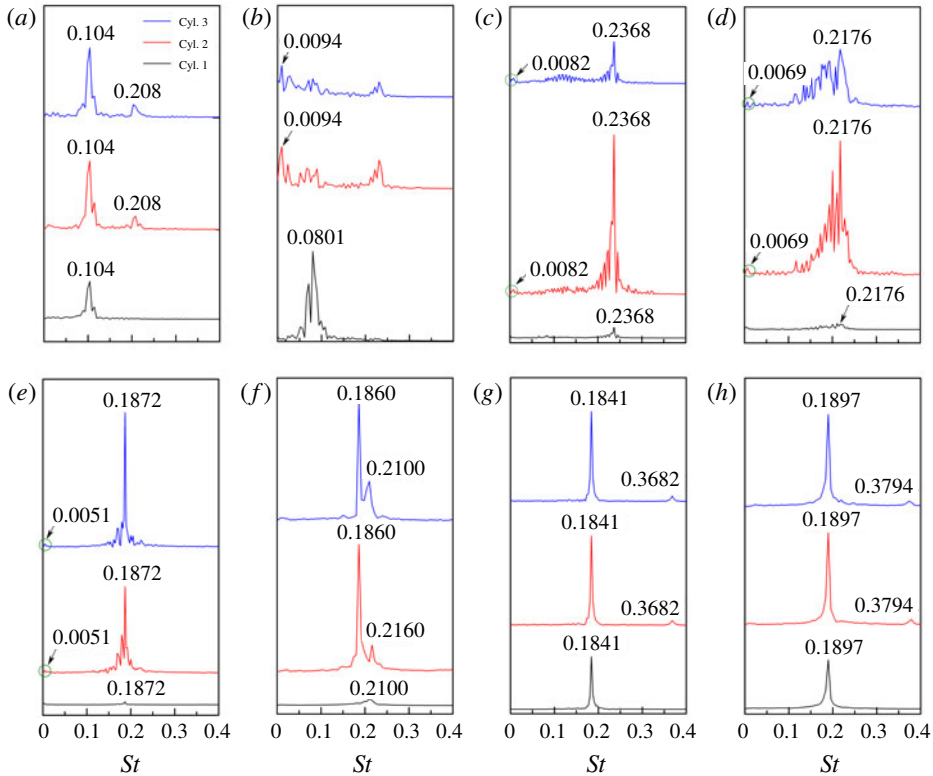


FIGURE 29. Spectral analyses of the lift coefficients of three cylinders at  $Re = 300$  and (a)  $L/D = 1.2$ , (b)  $L/D = 1.6$ , (c)  $L/D = 2.0$ , (d)  $L/D = 2.5$ , (e)  $L/D = 3.0$ , (f)  $L/D = 3.5$ , (g)  $L/D = 4.0$  and (h)  $L/D = 5.0$ .

fluid–structure interactions. Results are validated for three 2-D cases, including an isolated cylinder, two side-by-side cylinders and three cylinders, and one 3-D case. The focus is on the effects of  $L/D$ ,  $Re$  and three-dimensionality on the fluid dynamics, including wake structures, drag and lift coefficients and the Strouhal number.

At  $Re = 100$ , six distinct flow patterns, depending on  $L/D$ , are observed: single bluff-body flow ( $L/D = 1.0$ – $1.4$ ), deflected flow ( $L/D = 1.5$ – $1.9$ ), flip-flopping flow ( $L/D = 2.0$ – $2.5$ ), anti-phase flow ( $L/D = 2.6$ – $2.8$  and  $3.5$ – $4.1$ ), in-phase flow ( $L/D = 2.9$ – $3.4$  and  $4.2$ – $4.5$ ) and fully developed in-phase co-shedding flow ( $L/D = 4.6$ – $6.0$ ). In SB flow, the shear layers of the upstream cylinder encircle the downstream cylinders and vortex shedding occurs only from the free-stream sides of the two downstream cylinders. On the other hand, the IC flow features the vortex shedding from both free-stream and gap sides of the two downstream cylinders. With increasing  $L/D$  from SB to IC flow, strong interactions between upstream-cylinder-generated shear layers and downstream cylinders lead to the formation of DF, FF, IP and AP flow patterns. When the variation of  $Re = 50$ – $175$  is considered, three extra wake patterns emerge, including steady symmetric flow, steady asymmetric flow and hybrid flow. While there is no vortex shedding for the former two patterns, the latter consists of FF and AP flows that come one after another.

A map of the flow regimes in the  $Re - L/D$  parametric plane has been presented. The SB flow takes place at small  $L/D$  ( $< 1.25$ – $1.9$ , depending on  $Re$ ), while the IC

flow appears at large  $L/D$  ( $> 3.75$ – $6.0$ , depending on  $Re$ ) and large  $Re$  ( $> 70$ ). At low  $Re$  ( $< 100$ ) and low  $L/D$  ( $= 1.5$ – $3.2$ ), the SS and SA flows materialize. With  $Re > 75$ , when  $L/D$  is slightly increased from SB flow, the DF flow comes into being. An increase in  $L/D$  or  $Re$  from DF flow leads to FF flow because of the intensified interaction between the gap-side shear layers. With a further increase in  $L/D$ , the FF flow transmutes into IP flow or AP flow or HB flow depending on  $Re$ .

The parameters  $L/D$  and  $Re$  have significant influence on the hydrodynamics of three cylinders. The hydrodynamic force coefficients of the downstream cylinders are the same, except in the SA and DF regimes. At a given  $Re$ , the value of  $\bar{C}_d$  of the upstream cylinder firstly decreases and then increases with increasing  $L/D$ , while that of the downstream cylinders monotonically grows. The  $\bar{C}_d$  of each cylinder is more sensitive to  $L/D$  than  $Re$ . Although not as strong as  $L/D$ , the influence of  $Re$  on  $\bar{C}_d$  largely appears at small  $Re$  ( $< 125$ ). A minimum  $\bar{C}_d$  of the downstream cylinders occurs at  $L/D = 1.0$ ,  $Re = 50$ . The value of  $\bar{C}_l$  of the upstream cylinder is nearly zero for all flow patterns. The downstream cylinders have attractive  $\bar{C}_l$  in the IP, AP, FF and HB regimes and repulsive  $\bar{C}_l$  in the SB, DF, SS and IC regimes. The  $Re$  effect on  $\bar{C}_l$  is less prominent than  $L/D$ . The values of  $C'_d$  and  $C'_l$  are small at low  $Re$ , increasing with increasing  $Re$  for all three cylinders. The largest  $C'_d$  occurs at  $Re = 150$ ,  $L/D = 1.0$  while the largest  $C'_l$  exists at  $Re = 175$ ,  $L/D = 4.3$ . The value of  $C'_l$  of the upstream cylinder is trivial in the attractive  $\bar{C}_l$  region owing to the non-swinging shear layers in the gap. In the IC regime, the value of  $C'_l$  of the upstream cylinder is largely dependent on  $Re$  while those of the downstream cylinders are on both  $Re$  and  $L/D$ .

The 3-D wake at  $Re = 300$  exemplifies the SB ( $L/D = 1.2$ ), DF ( $L/D = 1.6$ ), FF ( $L/D = 2.0$ – $2.5$ ), HB ( $L/D = 3.0$ ) and IC ( $L/D \geq 3.5$ ) flows. These flow patterns are similar to those in the 2-D flow ( $Re < 175$ ), despite abundant streamwise vortical filaments developing in the wake at  $Re = 300$ . Due to the presence of the 3-D vortical structures along the cylinder, the fluid forces are generally smaller in the 3-D simulations than in two dimensions.

In this study, we systematically investigated the features of different flow regimes of three equilaterally arranged circular cylinders. Hydrodynamic forces, flow profiles, vortex-shedding frequencies, phase lags, wake patterns, together with the underlying physics, are discussed in depth. Compared with the previous studies, much finer resolutions in  $Re$  and  $L/D$  are adopted. As a result, a map of the flow regimes in the parametric plane  $Re - L/D$  is presented with distinct boundaries. This map is 'of primary importance for future linear and nonlinear stability analyses addressing the phase-space structure and dynamics of the considered flow configuration'. Another novelty of the present study is that we have done an investigation for a wide range of  $Re$  ( $= 50$ – $300$ ), covering both laminar and turbulent flows. The results are crucial to understanding the flow interferences between three circular cylinders in equilateral-triangular arrangements.

### Acknowledgements

This work was financially supported by the National Natural Science Foundation of China (grant nos 51579175, 51779172 and 51979186), the Science Fund for Creative Research Groups of the National Natural Science Foundation of China (grant no. 51621092). The National Key Research and Development Program of China (grant no. 2017YFC1404200). The work was carried out at National Supercomputer Center in Tianjin, and the calculations were performed in Tianhe 3 prototype. The first two authors acknowledge Dr H. An of The University of Western Australia for his constructive suggestions.

	$\bar{C}_d$	$C_l$	$St$
Persillon & Braza (1998)	1.366	0.477	0.206
Behara & Mittal (2010)	1.390	0.594	0.210
Zhao <i>et al.</i> (2013)	1.274	0.428	0.196
Jiang <i>et al.</i> (2016a)	1.291	0.464	0.204
Wieselsberger (1921)	1.208	—	—
Williamson (1996a)	—	—	0.203
Present <sup>a</sup>	1.285	0.441	0.205
Present <sup>b</sup>	1.282	0.445	0.202
Present <sup>c</sup>	1.311	0.454	0.202

TABLE 5. Comparison of hydrodynamic forces of flow past a single circular cylinder at  $Re = 300$ . The time step size is  $\Delta tU/D = 0.004$  in *a* and *c*, while  $\Delta tU/D = 0.002$  in *b*. The computational domain in the  $x$ - $y$  plane is  $100D$  (streamwise)  $\times$   $100D$  (transverse) in *a* and *c*, and  $50D \times 40D$  in *b*.

### Declaration of interests

The authors report no conflict of interest.

### Appendix

To verify the accuracy of the numerical methodology, three-dimensional simulations of flow past a single circular cylinder were carried out. The adopted computational domain size is  $100D$  in both streamwise and transverse directions, which has been verified to be sufficiently large (Jiang *et al.* 2016a,b; Jiang & Cheng 2017; Gao *et al.* 2019). The mesh resolution in the  $x$ - $y$  plane is the same as that in the two-dimensional simulations. In the spanwise ( $z$ -direction) direction, the cylinder length is  $12D$ , long enough for the adopted  $Re$  (Jiang *et al.* 2016a,b; Gao *et al.* 2019). A uniform mesh is applied in the  $z$  direction with a resolution of  $\Delta z = 0.0625D$ . Previous studies (Jiang *et al.* 2016a; Jiang & Cheng 2017) showed that  $\Delta z = 0.1D$  is fine enough for capturing the three-dimensional vortical structures at  $Re = 300$ . The validation of the results at  $Re = 300$  is provided in table 5. The present results show good agreements with the numerical and experimental data in the literature.

In addition, the convergence of the computational domain and time step sizes are examined. As shown in table 5, the results at  $\Delta tU/D = 0.004$  (case a) and  $\Delta tU/D = 0.002$  (case b) are close to each other, suggesting that the adopted time step  $\Delta tU/D = 0.004$  is small enough. The comparison of cases a and c indicates the adopted computational domain size  $100D$  (streamwise)  $\times$   $100D$  (transverse) in the  $x$ - $y$  plane is appropriate.

### REFERENCES

- AKBARI, M. H. & PRICE, S. J. 2005 Numerical investigation of flow patterns for staggered cylinder pairs in cross-flow. *J. Fluids Struct.* **20**, 533–554.
- AKILLI, H., AKAR, A. & KARAKUS, C. 2004 Flow characteristics of circular cylinders arranged side-by-side in shallow water. *Flow Meas. Instrum.* **15**, 187–197.
- ALAM, M. M. 2014 The aerodynamics of a cylinder submerged in the wake of another. *J. Fluids Struct.* **51**, 393–400.

- ALAM, M. M. 2016 Lift forces induced by the phase lag between the vortex sheddings from two tandem bluff bodies. *J. Fluids Struct.* **65**, 217–237.
- ALAM, M. M. & MEYER, J. P. 2013 Global aerodynamic instability of twin cylinders in cross flow. *J. Fluids Struct.* **41**, 135–145.
- ALAM, M. M., MORIYA, M. & SAKAMOTO, H. 2003a Aerodynamic characteristics of two side-by-side circular cylinders and application of wavelet analysis on the switching phenomenon. *J. Fluids Struct.* **18**, 325–346.
- ALAM, M. M., MORIYA, M., TAKAI, K. & SAKAMOTO, H. 2003b Fluctuating fluid forces acting on two circular cylinders in a tandem arrangement at a subcritical Reynolds number. *J. Wind Engng Ind. Aerodyn.* **91**, 139–154.
- ALAM, M. M. & SAKAMOTO, H. 2005 Investigation of Strouhal frequencies of two staggered bluff bodies and detection of multistable flow by wavelets. *J. Fluids Struct.* **20** (3), 425–449.
- ALAM, M. M. & ZHOU, Y. 2007 Phase lag between vortex sheddings from two tandem bluff bodies. *J. Fluids Struct.* **23**, 339–347.
- ALAM, M. M., ZHOU, Y. & WANG, X. W. 2011 The wake of two side-by-side square cylinders. *J. Fluid Mech.* **669**, 432–471.
- BANSAL, M. S. & YARUSEVYCH, S. 2017 Experimental study of flow through a cluster of three equally spaced cylinders. *Exp. Therm. Fluid Sci.* **80**, 203–217.
- BAO, Y., ZHOU, D. & HUANG, C. 2010 Numerical simulation of flow over three circular cylinders in equilateral arrangements at low Reynolds number by a second-order characteristic-based split finite element method. *Comput. Fluids* **39** (5), 882–899.
- BAO, Y., ZHOU, D. & TU, J. 2013 Flow characteristics of two in-phase oscillating cylinders in side-by-side arrangement. *Comput. Fluids* **71**, 124–145.
- BARKLEY, D. & HENDERSON, R. D. 1996 Three-dimensional floquet stability analysis of the wake of a circular cylinder. *J. Fluid Mech.* **322**, 215–241.
- BEARMAN, P. W. & WADCOCK, A. J. 1973 The interaction between a pair of circular cylinders normal to a stream. *J. Fluid Mech.* **61**, 499–511.
- BEHARA, S. & MITTAL, S. 2010 Wake transition in flow past a circular cylinder. *Phys. Fluids* **22**, 114104.
- BERGER, E. & WILLE, R. 1972 Periodic flow phenomena. *Annu. Rev. Fluid Mech.* **4**, 313–340.
- BREDE, M., ECKELMANN, H. & ROCKWELL, D. 1996 On secondary vortices in the cylinder wake. *Phys. Fluids* **8**, 2117–2124.
- CARINI, M., AUTERI, F. & GIANNETTI, F. 2015 Centre-manifold reduction of bifurcating flows. *J. Fluid Mech.* **767**, 109–145.
- CARINI, M., GIANNETTI, F. & AUTERI, F. 2014a First instability and structural sensitivity of the flow past two side-by-side cylinders. *J. Fluid Mech.* **749**, 627–648.
- CARINI, M., GIANNETTI, F. & AUTERI, F. 2014b On the origin of the flip–flop instability of two side-by-side cylinder wakes. *J. Fluid Mech.* **742**, 552–576.
- CARMO, B. S., MENEGHINI, J. R. & SHERWIN, S. J. 2010 Possible states in the flow around two circular cylinders in tandem with separations in the vicinity of the drag inversion spacing. *Phys. Fluids* **22** (5), 054101.
- CHEN, W., JI, C., WANG, R., XU, D. & CAMPBELL, J. 2015a Flow-induced vibrations of two side-by-side circular cylinders: Asymmetric vibration, symmetry hysteresis and near-wake patterns. *Ocean Engng* **110**, 244–257.
- CHEN, W., JI, C., WILLIAMS, J., XU, D., YANG, L. & CUI, Y. 2018 Vortex-induced vibrations of three tandem cylinders in laminar cross-flow: Vibration response and galloping mechanism. *J. Fluids Struct.* **78**, 215–238.
- CHEN, W., JI, C. & XU, D. 2019 Vortex-induced vibrations of two side-by-side circular cylinders with two degrees of freedom in laminar cross-flow. *Comput. Fluids* **193**, 104288.
- CHEN, W., JI, C., XU, W., LIU, S. & CAMPBELL, J. 2015b Response and wake patterns of two side-by-side elastically supported circular cylinders in uniform laminar cross-flow. *J. Fluids Struct.* **55**, 218–236.

- DADMARZI, F. H., NARASIMHAMURTHY, V. D., ANDERSSON, H. I. & PETTERSEN, B. 2018 Turbulent wake behind side-by-side flat plates: computational study of interference effects. *J. Fluid Mech.* **855**, 1040–1073.
- ESFAHANI, J. A. & VASEL-BE-HAGH, A. R. 2010 A Lattice Boltzmann simulation of cross-flow around four cylinders in a square arrangement. In *ASME 2010 10th Biennial Conference on Engineering Systems Design and Analysis, ESDA2010, Istanbul, Turkey*.
- ESFAHANI, J. A. & VASEL-BE-HAGH, A. R. 2013 A numerical study on shear layer behaviour in flow over a square unit of four cylinders at Reynolds number of 200 using the LB method. *Prog. Comput. Fluid Dyn.* **13** (2), 103–119.
- ÉTIENNE, S. & PELLETIER, D. 2012 The low Reynolds number limit of vortex-induced vibrations. *J. Fluids Struct.* **31**, 18–29.
- FARGE, M. 1992 Wavelet transforms and their applications to turbulence. *Annu. Rev. Fluid Mech.* **24**, 395–458.
- GAO, Y., QU, X., ZHAO, M. & WANG, L. 2019 Three-dimensional numerical simulation on flow past three circular cylinders in an equilateral-triangular arrangement. *Ocean Engng* **189**, 106375.
- HAN, Z., ZHOU, D. & TU, J. 2013 Laminar flow patterns around three side-by-side arranged circular cylinders using semi-implicit three-step Taylor-characteristic-based-split (3-TCBS) algorithm. *Eng. Appl. Comput. Fluids Mech.* **7** (1), 1–12.
- HARICHANDAN, A. B. & ROY, A. 2010 Numerical investigation of low Reynolds number flow past two and three circular cylinders using unstructured grid CFR scheme. *Intl J. Heat Fluid Flow* **31** (2), 154–171.
- HUERRE, P. & MONKEWITZ, P. A. 1990 Local and global instabilities in spatially developing flows. *Annu. Rev. Fluid Mech.* **22**, 473–537.
- IGARASHI, T. 1981 Characteristics of the flow around two circular cylinders arranged in tandem: 1st report. *Bull. JSME* **24**, 323–331.
- IGARASHI, T. & SUZUKI, K. 1984 Characteristics of the flow around three circular cylinders. *Bull. JSME* **27**, 2397–2404.
- JI, C., MUNJIZA, A. & WILLIAMS, J. J. R. 2012 A novel iterative direct-forcing immersed boundary method and its finite volume applications. *J. Comput. Phys.* **231** (4), 1797–1821.
- JIANG, H. & CHENG, L. 2017 Strouhal–Reynolds number relationship for flow past a circular cylinder. *J. Fluid Mech.* **832**, 170–188.
- JIANG, H., CHENG, L., DRAPER, S., AN, H. & TONG, F. 2016a Three-dimensional direct numerical simulation of wake transitions of a circular cylinder. *J. Fluid Mech.* **801**, 353–391.
- JIANG, H., CHENG, L., TONG, F., DRAPER, S. & AN, H. 2016b Stable state of mode a for flow past a circular cylinder. *Phys. Fluids* **28**, 104103.
- KANG, S. 2003 Characteristics of flow over two circular cylinders in a side-by-side arrangement at low Reynolds numbers. *Phys. Fluids* **15** (9), 2486–2498.
- KANG, S. 2004 Numerical study on laminar flow over three side-by-side cylinders. *KSME Int. J.* **18** (10), 1869–1879.
- KIM, H. J. & DURBIN, P. A. 1988 Investigation of the flow between a pair of circular cylinders in the flopping regime. *J. Fluid Mech.* **196**, 431–448.
- KUMAR, B. & MITTAL, S. 2006 Prediction of the critical Reynolds number for flow past a circular cylinder. *Comput. Meth. Appl. Mech. Engng* **195**, 6046–6058.
- LAM, K. & CHEUNG, W. C. 1988 Phenomena of vortex shedding and flow interference of three cylinders in different equilateral arrangements. *J. Fluid Mech.* **196**, 1–26.
- LAM, K., LI, J. Y. & SO, R. M. C. 2003 Force coefficients and Strouhal numbers of four cylinders in cross flow. *J. Fluids Struct.* **18**, 305–324.
- LEE, D. S., HA, M. Y., YOON, H. S. & BALACHANDAR, S. 2009 A numerical study on the flow patterns of two oscillating cylinders. *J. Fluids Struct.* **25** (2), 263–283.
- LI, Y., ZHANG, R., SHOCK, R. & CHEN, H. 2009 Prediction of vortex shedding from a circular cylinder using a volumetric Lattice-Boltzmann boundary approach. *Eur. Phys. J.* **171** (1), 91–97.

- LIU, C. H. & CHEN, J. M. 2002 Observations of hysteresis in flow around two square cylinders in a tandem arrangement. *J. Wind Engng Ind. Aerodyn.* **90** (9), 1019–1050.
- LIU, K., MA, D., SUN, D. & YIN, X. 2007 Wake patterns of flow past a pair of circular cylinders in side-by-side arrangements at low Reynolds numbers. *J. Hydrodyn. B* **19** (6), 690–697.
- LJUNGKRONA, L., NORBERG, C. H. & SUNDEN, B. 1991 Free-stream turbulence and tube spacing effects on surface pressure fluctuations for two tubes in an in-line arrangement. *J. Fluids Struct.* **5** (6), 701–727.
- MITTAL, S. 2005 Excitation of shear layer instability in flow past a cylinder at low Reynolds number. *Intl J. Numer. Meth. Fluids* **49** (10), 1147–1167.
- MITTAL, R. & BALAKANDAR, S. 1995 Generation of streamwise vortical structures in bluff body wakes. *Phys. Rev. Lett.* **75**, 1300–1303.
- MILLER, G. D. & WILLIAMSON, C. H. K. 1994 Control of three-dimensional phase dynamics in a cylinder wake. *Exp. Fluids* **18** (1–2), 26–35.
- MIZUSHIMA, J. & INO, Y. 2008 Stability of flows past a pair of circular cylinders in a side-by-side arrangement. *J. Fluid Mech.* **595**, 491–507.
- PAPAIOANNOU, G. V., YUE, D. K. P., TRIANTAFYLLOU, M. S. & KARNIADAKIS, G. E. 2006 Three-dimensionality effects in flow around two tandem cylinders. *J. Fluid Mech.* **558**, 387–413.
- PARK, J., KWON, K. & CHOI, H. 1998 Numerical solutions of flow past a circular cylinder at Reynolds numbers up to 160. *KSME Int. J.* **12** (6), 1200–1205.
- DE PAULA, A. V., ENDRES, L. A. M. & MÖLLER, S. V. 2013 Experimental study of the bistability in the wake behind three cylinders in triangular arrangement. *J. Braz. Soc. Mech. Sci. Engng* **35** (2), 163–176.
- PERSILLON, H. & BRAZA, M. 1998 Physical analysis of the transition to turbulence in the wake of a circular cylinder by three-dimensional Navier–Stokes simulation. *J. Fluid Mech.* **365**, 23–88.
- PESKIN, C. S. 1972 Flow patterns around heart valves: a numerical method. *J. Comput. Phys.* **10** (2), 252–271.
- POSDZIECH, O. & GRUNDMANN, R. 2001 Numerical simulation of the flow around an infinitely long circular cylinder in the transition regime. *Theor. Comput. Fluid Dyn.* **15** (2), 121–141.
- QU, L., NORBERG, C., DAVIDSON, L., PENG, S. & WANG, F. 2013 Quantitative numerical analysis of flow past a circular cylinder at Reynolds number between 50 and 200. *J. Fluids Struct.* **39**, 347–370.
- RIGONI, A. 2015 Linear stability analysis of the asymmetric base flow of two cylinders in side-by-side arrangement. MSc thesis, Polytechnic University of Milan.
- SAYERS, A. T. 1990 Vortex shedding from groups of three and four equispaced cylinders situated in a cross flow. *J. Wind Engng Ind. Aerodyn.* **34** (2), 213–221.
- SEN, S., MITTAL, S. & BISWAS, G. 2009 Steady separated flow past a circular cylinder at low Reynolds numbers. *J. Fluid Mech.* **620**, 89–119.
- SUMNER, D. 2010 Two circular cylinders in cross-flow: a review. *J. Fluids Struct.* **26** (6), 849–899.
- SUMNER, D., WONG, S. S. T., PRICE, S. J. & PAIDOUSSIS, M. P. 1999 Fluid behaviour of side-by-side circular cylinders in steady cross-flow. *J. Fluids Struct.* **13**, 309–338.
- SUPRADEEPAN, K. & ROY, A. 2014 Characterisation and analysis of flow over two side by side cylinders for different gaps at low Reynolds number: a numerical approach. *Phys. Fluids* **26** (6), 063602.
- TATSUNO, M., AMAMOTO, H. & ISHI-I, K. 1998 Effects of interference among three equidistantly arranged cylinders in a uniform flow. *Fluid Dyn. Res.* **22** (5), 297.
- TONG, F., CHENG, L. & ZHAO, M. 2015 Numerical simulations of steady flow past two cylinders in staggered arrangements. *J. Fluid Mech.* **765**, 114–149.
- WIESELSBERGER, E. 1921 Neuere Feststellungen über die Gesetze des Flüssigkeits und Luftwiderstand. *Physik. Z.* **22**, 321.
- WILLIAMSON, C. H. K. 1985 Evolution of a single wake behind a pair of bluff bodies. *J. Fluid Mech.* **159**, 1–18.
- WILLIAMSON, C. H. K. 1989 Oblique and parallel modes of vortex shedding in the wake of a circular cylinder at low Reynolds numbers. *J. Fluid Mech.* **206**, 579–627.

- WILLIAMSON, C. H. K. 1996*a* Three-dimensional wake transition. *J. Fluid Mech.* **328**, 345–407.
- WILLIAMSON, C. H. K. 1996*b* Vortex dynamics in the cylinder wake. *Annu. Rev. Fluid Mech.* **28**, 477–539.
- WOOD, C. J. 1967 Visualization of incompressible wake with base bleed. *J. Fluid Mech.* **29** (2), 259–272.
- YANG, S., YAN, W., WU, J., TU, C. & LUO, D. 2016 Numerical investigation of vortex suppression regions for three staggered circular cylinders. *Eur. J. Mech. (B/Fluids)* **55**, 207–214.
- ZDRAVKOVICH, M. M. 1977 Review of flow interference between two circular cylinders in various arrangements. *Trans. ASME J. Fluids Engng* **90**, 618–633.
- ZDRAVKOVICH, M. M. 1987 The effects of flow interference between two circular cylinders in various arrangements. *J. Fluids Struct.* **1**, 239–261.
- ZDRAVKOVICH, M. M. 1997 *Flow Around Circular Cylinders*. Oxford University Press.
- ZHAO, M., CHENG, L. & AN, H. 2012 Numerical investigation of vortex-induced vibration of a circular cylinder in transverse direction in oscillatory flow. *Ocean Engng* **41**, 39–52.
- ZHAO, M., THAPA, J., CHENG, L. & ZHOU, T. 2013 Three-dimensional transition of vortex shedding flow around a circular cylinder at right and oblique attacks. *Phys. Fluids* **25**, 014105.
- ZHENG, S., ZHANG, W. & LV, X. 2016 Numerical simulation of cross-flow around three equal diameter cylinders in an equilateral-triangular configuration at low Reynolds numbers. *Comput. Fluids* **130**, 94–108.